AN ULTRAVIOLET-TO-RADIO BROADBAND SPECTRAL ATLAS OF NEARBY GALAXIES

D. A. Dale,[1] A. Gil de Paz,[2] K. D. Gordon,[3] H. M. Hanson,[1] L. Armus,[4] G. J. Bendo,[5] L. Bianchi,[6] M. Block,[3]
S. Boissier,[7,8] A. Boselli,[8] B. A. Buckalew,[9] V. Buat,[8] D. Burgarella,[8] D. Calzetti,[10] J. M. Cannon,[11]
C. W. Engelbracht,[3] G. Helou,[9] D. J. Hollenbach,[12] T. H. Jarrett,[4] R. C. Kennicutt,[3,13]
C. Leitherer,[10] A. Li,[14] B. F. Madore,[7] D. C. Martin,[15] M. J. Meyer,[10]
E. J. Murphy,[16] M. W. Regan,[10] H. Roussel,[17] J. D. T. Smith,[3]
M. L. Sosey,[10] D. A. Thilker,[6] and F. Walter[17]

ABSTRACT

The ultraviolet-to-radio continuum spectral energy distributions are presented for all 75 galaxies in the *Spitzer* Infrared Nearby Galaxies Survey (SINGS). A principal component analysis of the sample shows that most of the sample's spectral variations stem from two underlying components, one representative of a galaxy with a low infrared-to-ultraviolet ratio and one representative of a galaxy with a high infrared-to-ultraviolet ratio. The influence of several parameters on the infrared-to-ultraviolet ratio is studied (e.g., optical morphology, disk inclination, far-infrared color, ultraviolet spectral slope, and star formation history). Consistent with our understanding of normal star-forming galaxies, the SINGS sample of galaxies in comparison to more actively star-forming galaxies exhibits a larger dispersion in the infrared-to-ultraviolet versus ultraviolet spectral slope correlation. Early-type galaxies, exhibiting low star formation rates and high optical surface brightnesses, have the most discrepant infrared-to-ultraviolet correlation. These results suggest that the star formation history may be the dominant regulator of the broadband spectral variations between galaxies. Finally, a new discovery shows that the 24 μm morphology can be a useful tool for parameterizing the global dust temperature and ultraviolet extinction in nearby galaxies. The dust emission in dwarf/irregular galaxies is clumpy and warm accompanied by low ultraviolet extinction, while in spiral galaxies there is typically a much larger diffuse component of cooler dust and average ultraviolet extinction. For galaxies with nuclear 24 μm emission, the dust temperature and ultraviolet extinction are relatively high compared to disk galaxies.

Subject headings: galaxies: photometry — infrared: galaxies — infrared: ISM — ultraviolet: galaxies

Online material: color figures

1. INTRODUCTION

Interstellar dust has always presented challenges to astronomers. Extinction makes it difficult to extract intrinsic fluxes. Reddening leads to uncertain colors. An outstanding challenge is to identify dust absorption features (diffuse interstellar bands) that were discovered over 80 years ago. Nonetheless, interstellar dust also provides unique opportunities for understanding galaxy structure and evolution. The formation of molecules, interstellar heating and cooling processes, polarization, and photometric redshift indicators are just a few of the areas of study that benefit from the presence and knowledge of interstellar grains (for a review see Draine 2003).

Although dust primarily releases energy over infrared and submillimeter wavelengths, much of the radiation intercepted by interstellar grains originates in the ultraviolet from the atmospheres of OB stars. Thus, the combination of infrared and ultraviolet data should provide a powerful diagnostic of star formation and selective extinction. One important application is determining ultraviolet-based star formation rates corrected for dust extinction. High-redshift surveys carried out in the rest-frame ultraviolet and optical, for example, are particularly vulnerable to the presence of interstellar dust (e.g., Adelberger & Steidel 2000). Fortunately, studies coupling infrared and ultraviolet data have shown that the slope of the ultraviolet continuum is one such useful probe of the extinction in starburst galaxies (e.g., Calzetti et al. 1994; Meurer et al. 1999). Subsequent work in this area has explored how the infrared-to-ultraviolet ratio and its scatter depend on bolometric and monochromatic luminosity, ultraviolet spectral slope, metallicity, diameter, star formation rate, etc. (e.g., Gordon et al. 2000, 2004; Buat et al. 2002, 2005; Bell 2003; Kong et al. 2004; Burgarella et al. 2005; Calzetti et al. 2005; Seibert et al. 2005; Cortese et al. 2006; Schmitt et al. 2006; Iglesias-Páramo et al. 2006; Inoue et al. 2006). One consistent result relevant to the work presented here is that normal star-forming (nonstarburst) galaxies show larger scatter in plots of the infrared-to-ultraviolet ratio as a function of the ultraviolet spectral slope, with normal galaxies systematically exhibiting redder slopes than starburst galaxies. This broadening in the trend has been attributed to geometry, integrated versus local extractions, and/or the increased fractional

[1] Department of Physics and Astronomy, University of Wyoming, Laramie, WY; ddale@uwyo.edu.
[2] Departamento de Astrofisica, Universidad Complutense, Madrid, Spain.
[3] Steward Observatory, University of Arizona, Tucson, AZ.
[4] *Spitzer* Science Center, California Institute of Technology, Pasadena, CA.
[5] Astrophysics Group, Imperial College, Blackett Laboratory, London, UK.
[6] Center for Astrophysical Sciences, Johns Hopkins University, Baltimore, MD.
[7] Carnegie Observatories, Carnegie Institution of Washington, Pasadena, CA.
[8] Laboratoire d'Astrophysique de Marseille, Traverse du Siphon, Marseille, France.
[9] California Institute of Technology, Pasadena, CA.
[10] Space Telescope Science Institute, Baltimore, MD.
[11] Astronomy Department, Wesleyan University, Middletown, CT.
[12] NASA/Ames Research Center, Moffett Field, CA.
[13] Institute of Astronomy, University of Cambridge, Cambridge, UK.
[14] Department of Physics and Astronomy, University of Missouri, Columbia, MO.
[15] Astronomy Option, California Institute of Technology, Pasadena, CA.
[16] Department of Astronomy, Yale University, New Haven, CT.
[17] Max-Planck-Institut für Astronomie, Heidelberg, Germany.

TABLE 1
GALAXY DATA

Galaxy	Optical Morphology	α_0 (J2000.0)	δ_0 (J2000.0)	$2a$ (arcsec)	$2b$ (arcsec)	P.A. (deg)	$f_\nu(24)[\text{unres}]/f_\nu(24)[\text{res}]^a$	$f_\nu(24)[\text{nuc}]/f_\nu(24)[\text{total}]^a$	θ_{FUV}^b (arcsec)
NGC 0024[†]	SAc	00 09 55.9	−24 57 55	301	216	135	0.31	0.14	36.0
NGC 0337[†]	SBd	00 59 50.7	−07 34 44	253	194	50	0.93	0.17	26.7
NGC 0584[†]	E4	01 31 20.6	−06 52 05	326	278	330	0.49	0.39	28.8
NGC 0628[†]	SAc	01 36 41.8	+15 47 17	721	717	248	0.84	0.01	150.
NGC 0855.................	E	02 14 03.9	+27 52 39	190	170	338	2.38	0.69	. . .
NGC 0925[†]	SABd	02 27 13.6	+33 35 04	735	486	15	0.71	0.02	114
NGC 1097[†]	SBb	02 46 18.0	−30 16 42	758	612	40	0.64	0.12	129
NGC 1266[†]	SB0	03 16 00.7	−02 25 41	234	232	0	9.09	0.87	10.5
NGC 1291[†]	SB0/a	03 17 19.1	−41 06 32	840	803	0	0.48	0.21	253
NGC 1316[†]	SAB0	03 22 41.2	−37 12 10	864	583	230	0.60	0.05	89.2
NGC 1377.................	S0	03 36 39.0	−20 54 08	181	162	0	∼20	0.85	. . .
NGC 1404.................	E1	03 38 52.3	−35 35 40	524	369	239	0.57	0.29	. . .
NGC 1482[†]	SA0	03 54 39.0	−20 30 09	349	310	29	5.26	0.77	19.0
NGC 1512[†]	SBab	04 03 55.0	−43 20 44	491	287	325	0.33	0.10	136
NGC 1566[†]	SABbc	04 20 00.4	−54 56 15	552	435	40	1.22	0.11	84.3
NGC 1705[†]	SA0	04 54 13.5	−53 21 37	167	120	130	1.03	0.43	. . .
NGC 2403[†]	SABcd	07 36 55.0	+65 35 54	1164	848	40	0.76	0.01	161
Holmberg II[†]	Im	08 19 06.8	+70 43 09	441	430	0	1.67	0.01	119
M81 Dwarf A	I?	08 23 56.0	+71 01 45	78	78	0	. . .	. . .	. . .
DDO 053[†]	Im	08 34 06.8	+66 10 36	133	110	30	7.69	0.08	22.9
NGC 2798[†]	SBa	09 17 23.1	+41 59 57	235	232	0	>10	0.75	7.8
NGC 2841[†]	SAb	09 22 03.3	+50 58 37	550	342	150	0.22	0.04	74.2
NGC 2915[†]	I0	09 26 09.4	−76 37 36	183	132	290	1.56	0.53	. . .
Holmberg I[†]	IABm	09 40 30.5	+71 10 33	265	228	120	0.28	0.01	59.9
NGC 2976[†]	SAc	09 47 15.3	+67 55 07	457	311	322	1.12	0.05	45.2
NGC 3049.................	SBab	09 54 49.6	+09 16 14	218	160	119	5.88	0.74	. . .
NGC 3031.................	SAab	09 55 31.8	+69 04 03	1628	1122	154	0.52	0.07	324
NGC 3034[c]	I0	. . .	. . .	. . .	. . .	. . .	. . .	. . .	. . .
Holmberg IX.............	Im	09 57 29.2	+69 02 50	247	180	130	. . .	. . .	47.8
M81 Dwarf B[†]	Im	10 05 31.3	+70 21 52	107	69	140	1.61	0.50	. . .
NGC 3190[†]	SAap	10 18 05.7	+21 49 57	334	196	117	1.59	0.35	29.2
NGC 3184.................	SABcd	10 18 15.6	+41 25 42	614	538	349	0.73	0.01	. . .
NGC 3198.................	SBc	10 19 54.8	+45 33 01	518	315	125	1.32	0.34	. . .
IC 2574[†]	SABm	10 28 22.7	+68 24 48	827	376	140	1.02	0.03	188
NGC 3265[†]	E	10 31 06.8	+28 47 51	184	175	320	8.33	0.82	. . .
Mrk 33[†]	Im	10 32 31.2	+54 23 59	181	177	0	8.33	0.75	. . .
NGC 3351[†]	SBb	10 43 57.5	+11 42 19	586	457	10	1.82	0.46	84.5
NGC 3521[†]	SABbc	11 05 48.7	−00 02 22	766	494	342	0.35	0.04	89.6
NGC 3621.................	SAd	11 18 18.3	−32 48 55	791	555	340	0.56	0.02	125
NGC 3627[†]	SABb	11 20 13.4	+12 59 27	745	486	347	0.90	0.01	56.0
NGC 3773[†]	SA0	11 38 13.1	+12 06 44	96	94	0	9.09	0.85	. . .
NGC 3938.................	SAc	11 52 50.3	+44 07 15	504	468	0	0.58	0.04	. . .
NGC 4125.................	E6p	12 08 05.8	+65 10 24	228	151	0	0.56	0.40	. . .
NGC 4236[†]	SBdm	12 16 35.9	+69 28 08	1129	420	155	1.92	0.004	169
NGC 4254.................	SAc	12 18 49.7	+14 25 19	519	420	330	0.48	0.03	. . .
NGC 4321.................	SABbc	12 22 54.8	+15 49 07	558	483	310	0.29	0.09	. . .
NGC 4450.................	SAab	12 28 30.1	+17 04 54	401	284	0	0.57	0.08	. . .
NGC 4536[†]	SABbc	12 34 27.5	+02 11 13	454	376	30	3.45	0.48	79.4
NGC 4552.................	E	12 35 39.8	+12 33 23	306	306	0	0.41	0.52	13.3
NGC 4559[†]	SABcd	12 35 58.1	+27 57 52	576	327	50	0.83	0.04	87.1
NGC 4569.................	SABab	12 36 50.2	+13 10 01	593	327	21	1.30	0.10	59.2
NGC 4579[†]	SABb	12 37 43.6	+11 49 00	295	229	0	1.19	0.27	54.5
NGC 4594[†]	SAa	12 39 59.4	−11 37 14	554	232	0	0.19	0.15	61.0
NGC 4625[†]	SABmp	12 41 52.3	+41 16 18	198	190	140	0.55	0.21	28.1
NGC 4631[†]	SBd	12 42 03.7	+32 32 05	952	539	350	0.45	0.03	84.3
NGC 4725[†]	SABab	12 50 27.7	+25 29 48	689	523	30	0.51	0.01	124
NGC 4736[†]	SAab	12 50 56.7	+41 07 06	1033	824	10	0.65	0.07	40.7
DDO 154[†]	IBm	12 54 05.2	+27 08 54	198	126	123	1.16	0.00	33.2
NGC 4826.................	SAab	12 56 42.8	+21 40 50	722	448	112	0.32	0.14	41.2
DDO 165[†]	Im	13 06 25.0	+67 42 26	267	150	0	>10	0.05	41.7
NGC 5033.................	SAc	13 13 28.2	+36 35 34	729	467	0	0.36	0.12	. . .
NGC 5055.................	SAbc	13 15 48.3	+42 01 42	893	682	11	0.38	0.04	108
NGC 5194[†]	SABbc	13 29 50.6	+47 13 07	1699	1129	285	0.51	0.002	143
NGC 5195[†]	SB0p	13 29 59.4	+47 15 56	202	191	0	3.32	0.61	110
Tol 89	SBdm	14 01 21.3	−33 04 01	196	130	0	7.69	0.09	31.9
NGC 5408.................	IBm	14 03 21.1	−41 22 41	256	209	67	3.57	0.02	. . .

TABLE 1—*Continued*

Galaxy	Optical Morphology	α_0 (J2000.0)	δ_0 (J2000.0)	$2a$ (arcsec)	$2b$ (arcsec)	P.A. (deg)	$f_\nu(24)[\text{unres}]/f_\nu(24)[\text{res}]^{\text{a}}$	$f_\nu(24)[\text{nuc}]/f_\nu(24)[\text{total}]^{\text{a}}$	$\theta_{\text{FUV}}{}^{\text{b}}$ (arcsec)
NGC 5474[†]	SAcd	14 04 59.9	+53 39 13	386	335	120	0.68	0.04	84.3
NGC 5713[†]	SABbcp	14 40 11.2	−00 17 26	153	140	0	1.67	0.49	15.0
NGC 5866[†]	S0	15 06 28.8	+55 45 51	500	306	39	1.41	0.34	26.3
IC 4710	SBm	18 28 38.9	−66 59 03	313	219	30	1.89	0.03	...
NGC 6822[†]	IBm	19 44 53.2	−14 48 11	1453	1100	330	1.21	0.0005	257
NGC 6946..................	SABcd	20 34 52.0	+60 09 15	818	763	0	0.95	0.23	...
NGC 7331[†]	SAb	22 37 04.3	+34 24 35	683	335	78	0.30	0.06	83.3
NGC 7552[†]	SAc	23 16 10.8	−42 35 05	441	325	30	1.56	0.72	36.3
NGC 7793[†]	SAd	23 57 50.4	−32 35 30	754	498	0	0.67	0.03	109

Notes.—Units of right ascension are hours, minutes, and seconds, and units of declination are degrees, arcminutes, and arcseconds. The ellipse parameters used in extracting optical and infrared fluxes are listed above. The position angle is measured east of north. Daggers indicate that the galaxy was used in the principal component analysis (see § 4.3).

[a] See § 5.3. Entries are not included for NGC 3034 (saturated) and M81 Dwarf A and Holmberg IX (nondetections).
[b] The equivalent radius of the ellipse including half of the total far-ultraviolet light.
[c] The bright core of NGC 3034 (M82) has rendered the *Spitzer* data extremely difficult to process. Saturation effects severely limit our ability to extract reliable flux densities.

contributions from recent (vs. current) star formation (e.g., Bell et al. 2002; Kong et al. 2004; Calzetti et al. 2005; Seibert et al. 2005; Boissier et al. 2007).

We are interested in exploring how the infrared-to-ultraviolet ratio depends on quantities like optical and mid-infrared morphology, ultraviolet and far-infrared color, and geometry within the *Spitzer* Nearby Galaxies Survey (SINGS) sample (Kennicutt et al. 2003). But in broader terms, the main focus of this paper is to simply present a panchromatic atlas of the broadband spectral energy distributions (SEDs) of a large, diverse sample of nearby galaxies and to quantify the variety of spectral shapes evident in such a sample. Since the fluxes presented in this work span wavelengths from the far-ultraviolet to the radio and are integrated over entire galaxies, this data set should prove useful to astronomers studying galaxies at high redshifts, where only information on the global properties of galaxies is accessible and the rest-frame ultraviolet data are shifted into optical bandpasses. One may plausibly argue that the variety of luminosities and spectral shapes typically seen in high-redshift surveys will be different than the diversity presented below for the SINGS sample (e.g., $10^7 \lesssim L_{\text{IR}}/L_\odot \lesssim 10^{11}$), since flux-limited surveys at high redshifts will mainly be sampling luminous and infrared-warm systems. On the other hand, deep far-infrared surveys show significant numbers of higher redshift systems similar to local normal star-forming galaxies in mass, size, and dust temperature (e.g., Chapman et al. 2002; Sajina et al. 2006). In either case, the rich collection of *Spitzer*, *GALEX*, and ancillary data provided by the SINGS project represents an important panchromatic baseline for extragalactic work.

Some of the analysis presented below could be accomplished using existing data sets, for example, the *GALEX*+*UBV*+2MASS+ *IRAS* work of Gil de Paz et al. (2007). However, the sensitivity and angular resolution of our *Spitzer* observations allow us to probe the dust emission in both bright and faint galaxies, and to do so in a spatially resolved manner. The paper is outlined as follows. In § 2 we present the SINGS sample, while in § 3 we present the collection of ultraviolet, optical, near-infrared, infrared, submillimeter, and radio data. The analysis of the broadband SEDs is described in § 4, and the infrared-to-ultraviolet ratio is explored in detail in § 5. A discussion and summary of the main results are provided in § 6.

2. THE SAMPLE

The selection of the 75 galaxies in SINGS (Kennicutt et al. 2003) aimed to span a wide range in three key parameters (opti-

cal morphology, luminosity, infrared-to-optical ratio) and to adequately sample several other secondary parameters (e.g., infrared color, metallicity, surface brightness, inclination, bar structure). The SINGS sample is comprised of nearby galaxies, with a median distance of ∼10 Mpc and a maximum distance of 30 Mpc. SINGS galaxies come from a wide range of environments and galaxy types: low-metallicity dwarfs; quiescent elliptical galaxies; dusty grand-design spiral galaxies; Seyferts, LINERs, and star-forming nuclei of normal galaxies; systems within the Local Group and M81 group; and both field and (Virgo) cluster galaxies (Table 1).

3. THE DATA

Tables 2 and 3 present the global flux densities for the entire SINGS sample, for wavelengths spanning the ultraviolet through the radio. The data are corrected for Galactic extinction (Schlegel et al. 1998) assuming $A_V/E(B − V) \approx 3.1$ and the reddening curve of Li & Draine (2001). The effect of air mass has been removed from the ground-based fluxes. Below follows a description of the new ultraviolet and optical and archival radio data collected for the SINGS program, in addition to a few updates to the *Spitzer* data presented in Dale et al. (2005).

3.1. *Ultraviolet Data*

The *GALEX* mission (Martin et al. 2005) is performing an all-sky survey at ultraviolet wavelengths. The imaging portion of the survey is being carried out with a far-ultraviolet and a near-ultraviolet filter centered at 1528 and 2271 Å with respective FWHMs of 269 and 616 Å. In addition to imaging the entire sky with an effective exposure time of ∼0.1 ks, *GALEX* is also carrying out relatively deep integrations (∼1.5 ks) for a few hundred nearby galaxies, including nearly the entire SINGS sample. With an angular resolution of 4″–6″, the spatial details in *GALEX* images are well matched to those seen in *Spitzer* 24 μm imaging and more resolved than in *Spitzer* 70 and 160 μm images. At the median distance of the SINGS sample (∼10 Mpc), the *GALEX* and MIPS 24 μm data probe spatial scales of about ∼300 pc. This resolution, coupled with the *GALEX* field of view of 1.25°, allows for robust measures of sky-subtracted, spatially integrated ultraviolet fluxes even for large nearby galaxies.

Integrated ultraviolet fluxes are computed from the surface photometry profiles derived for the *GALEX* Atlas of Nearby Galaxies

TABLE 2
Ultraviolet, Optical, and Near-Infrared Flux Densities

Galaxy	$E(B-V)$ (mag)	FUV 1528 Å (mJy)	NUV 2271 Å (mJy)	B 0.45 μm (Jy)	V 0.55 μm (Jy)	R 0.66 μm (Jy)	I 0.81 μm (Jy)	J 1.25 μm (Jy)	H 1.65 μm (Jy)	K_s 2.17 μm (Jy)
NGC 0024	0.020	8.76 ± 1.21	11.43 ± 1.58	0.082	0.11	0.11	0.097	0.23	0.25	0.19
NGC 0337	0.112	10.46 ± 1.45	18.69 ± 2.59	0.11	0.12	0.10	0.085	0.20	0.20	0.17
NGC 0584	0.042	0.37 ± 0.05	2.00 ± 0.28	0.14	0.28	0.28	0.29	0.91	1.12	0.87
NGC 0628	0.070	75.96 ± 10.52	99.23 ± 13.74	0.65	0.84	0.76	0.65	1.66	1.67	1.32
NGC 0855	0.071	1.81 ± 0.25	3.25 ± 0.45	0.034[b]	0.047[b]	. . .	. . .	0.096	0.10	0.085
NGC 0925	0.076	50.99 ± 7.06	62.43 ± 8.65	0.35	0.48	0.59	0.62	0.60	0.65	0.51
NGC 1097	0.027	36.26 ± 5.19	50.97 ± 7.18	0.51	0.84	0.79	0.82	2.40	2.74	2.29
NGC 1266	0.098	0.049 ± 0.007	0.29 ± 0.04	0.020	0.036	0.037	0.035	0.12	0.13	0.12
NGC 1291	0.013	7.38 ± 1.02	16.28 ± 2.26	0.76	1.48	1.37	1.48	4.34	4.48	3.93
NGC 1316	0.021	3.13 ± 0.44	16.58 ± 2.30	0.79	1.61	1.58	1.73	4.69	4.90	4.21
NGC 1377	0.028	. . .	. . .	0.012	0.023	0.021	0.033	0.10	0.11	0.095
NGC 1404	0.011	0.97 ± 0.13	2.76 ± 0.38	0.24	0.48	0.48	0.49	1.38	1.59	1.35
NGC 1482	0.040	0.41 ± 0.06	1.43 ± 0.21	0.024	0.046	0.053	0.052	0.23	0.30	0.29
NGC 1512	0.011	14.95 ± 2.08	19.88 ± 2.77	0.13	0.25	0.26	0.21	0.81	0.86	0.73
NGC 1566	0.009	54.49 ± 7.59	65.52 ± 9.07	0.43	0.45	0.47	0.42	1.39	1.42	1.27
NGC 1705	0.008	16.01 ± 2.22	16.76 ± 2.32	0.037	0.042	0.036	0.028	0.057	0.054	0.044
NGC 2403	0.040	258.1 ± 35.7	307.5 ± 42.6	1.90	2.42	2.37	3.45	2.94	2.91	2.39
Holmberg II	0.032	47.80 ± 6.62	48.23 ± 6.68	0.21	0.19	0.25	0.38	0.22	0.34	0.26
M81 Dwarf A	0.020	0.48 ± 0.07	0.56 ± 0.08	0.002	0.001	0.001	0.002	0.004	0.004	0.003
DDO 053	0.038	2.65 ± 0.37	2.58 ± 0.36	0.011	0.008	0.006	0.007	0.008	0.014	0.008
NGC 2798	0.020	1.12 ± 0.16	2.33 ± 0.32	0.059	0.075	0.071	0.089	0.16	0.19	0.17
NGC 2841	0.015	12.99 ± 1.80	20.57 ± 2.85	0.85	1.00	1.26	1.40	2.81	3.22	2.67
NGC 2915	0.275	16.13 ± 2.23	16.43 ± 2.27	0.077[b]	0.069	0.071	0.077	0.13	0.15	0.092
Holmberg I	0.050	5.29 ± 0.73	5.60 ± 0.78	0.032	0.029	0.015	0.021	0.031	0.040	0.016
NGC 2976	0.071	18.86 ± 2.61	30.24 ± 4.19	0.52	0.47	0.52	0.61	0.86	0.89	0.71
NGC 3049[a]	0.038	. . .	4.51 ± 0.62	0.052	0.051	0.046	0.050	0.078	0.082	0.074
NGC 3031	0.080	178.9 ± 24.8	256.33 ± 35.49	5.07[b]	8.73[b]	. . .	. . .	23.47	25.44	21.29
NGC 3034	0.156	50.08 ± 6.93	105.3 ± 14.6	3.53	2.79[b]	3.67	4.74	9.24	10.80	10.14
Holmberg IX	0.079	4.01 ± 0.56	5.00 ± 0.69	0.014	0.010	0.008	0.010	0.025	0.021	0.015
M81 Dwarf B	0.081	0.75 ± 0.10	0.92 ± 0.13	0.009	0.007	0.007	0.007	0.012	0.014	0.014
NGC 3190	0.025	0.40 ± 0.06	1.80 ± 0.25	0.21	0.27	0.26	0.37	0.71	0.84	0.74
NGC 3184	0.017	. . .	. . .	0.67	0.71	0.70	1.10	1.05	1.14	0.91
NGC 3198	0.012	23.60 ± 3.27	28.38 ± 3.93	0.21	0.30	0.34	0.42	0.57	0.63	0.55
IC 2574	0.036	46.61 ± 6.45	48.37 ± 6.70	0.18	0.22	0.20	0.27	0.34	0.23	0.17
NGC 3265	0.024	0.57 ± 0.08	0.96 ± 0.13	0.021	0.024	0.012	0.024	0.051	0.057	0.048
Mrk 33	0.012	4.13 ± 0.57	5.20 ± 0.72	0.038	0.034	0.029	0.029	0.049	0.056	0.048
NGC 3351	0.028	17.66 ± 2.45	28.77 ± 3.98	0.45	0.58	0.71	0.98	1.68	1.77	1.54
NGC 3521	0.057	22.19 ± 3.07	44.66 ± 6.18	0.89	1.23	1.40	2.32	3.73	4.22	3.50
NGC 3621	0.081	76.91 ± 11.20	110.2 ± 15.8	0.62[b]	1.10	. . .	1.53	1.94	2.15	1.69
NGC 3627	0.033	30.46 ± 4.22	61.43 ± 8.51	1.51	1.63	1.51	1.90	3.34	3.73	3.17
NGC 3773	0.027	4.21 ± 0.58	5.55 ± 0.77	0.036	0.033	0.028	0.031	0.045	0.039	0.037
NGC 3938[a]	0.021	. . .	36.41 ± 5.04	0.44	0.44	0.34	0.41	0.64	0.58	0.54
NGC 4125[a]	0.019	. . .	3.44 ± 0.48	0.49	0.54	0.66	0.87	1.39	1.54	1.29
NGC 4236	0.015	63.45 ± 8.79	76.24 ± 10.56	0.42	0.53	0.62	0.54	0.63	0.83	0.57
NGC 4254[a]	0.039	. . .	61.82 ± 8.56	0.78	0.75	0.64	0.73	1.27	1.35	1.21
NGC 4321[a]	0.026	. . .	54.04 ± 7.48	0.50	0.70	0.85	1.23	1.87	2.00	1.65
NGC 4450[a]	0.028	. . .	5.39 ± 0.75	0.43	0.53	0.52	0.65	1.20	1.39	1.08
NGC 4536	0.018	16.94 ± 2.35	21.93 ± 3.04	0.40	0.42	0.47	0.51	0.71	0.75	0.70
NGC 4552	0.041	1.89 ± 0.26	4.66 ± 0.65	0.37	0.49	0.49	0.58	1.63	1.80	1.46
NGC 4559	0.018	53.79 ± 7.45	64.63 ± 8.95	0.66	0.50	0.50	0.58	0.77	0.79	0.66
NGC 4569	0.047	6.00 ± 0.83	19.69 ± 2.73	0.50[b]	0.72[b]	. . .	. . .	1.83	2.08	1.67
NGC 4579	0.041	5.85 ± 0.81	12.11 ± 1.68	0.73	0.76	0.87	1.18	2.05	2.24	1.82
NGC 4594	0.051	5.55 ± 0.77	17.72 ± 2.47	2.25	2.76	3.41	4.30	8.06	9.19	7.57
NGC 4625	0.018	6.04 ± 0.84	7.97 ± 1.10	0.073	0.071	0.061	0.071	0.098	0.11	0.089
NGC 4631	0.017	80.95 ± 11.21	104.8 ± 14.5	1.19	0.91	0.96	1.12	1.75	1.98	1.84
NGC 4725	0.012	22.05 ± 3.07	29.61 ± 4.13	0.54	0.89	1.04	1.48	2.43	3.18	2.41
NGC 4736	0.018	67.19 ± 9.30	91.87 ± 12.72	2.50	2.79	2.76	3.39	6.94	7.68	6.44
DDO 154	0.009	4.54 ± 0.63	4.42 ± 0.61	0.016	0.011	0.009	0.009	0.010	0.012	0.012
NGC 4826	0.041	14.50 ± 2.01	37.45 ± 5.19	1.41	2.05	. . .	. . .	5.67	6.30	5.28
DDO 165	0.024	6.72 ± 0.93	8.15 ± 1.13	0.041	0.034	0.024	0.023	0.026	0.017	0.010
NGC 5033	0.012	. . .	. . .	0.54	0.66	. . .	0.80	1.21	1.35	1.17
NGC 5055	0.018	39.30 ± 5.44	63.42 ± 8.78	1.08[b]	1.59[b]	. . .	. . .	4.21	4.96	4.05
NGC 5194	0.035	160.0 ± 22.2	260.8 ± 36.1	1.47	1.96	2.20	3.02	4.99	5.89	4.52
NGC 5195	0.035	3.36 ± 0.48	10.04 ± 1.40	0.37	0.62	0.81	1.51	2.37	2.80	2.26

TABLE 2—*Continued*

Galaxy	$E(B-V)$ (mag)	FUV 1528 Å (mJy)	NUV 2271 Å (mJy)	B 0.45 μm (Jy)	V 0.55 μm (Jy)	R 0.66 μm (Jy)	I 0.81 μm (Jy)	J 1.25 μm (Jy)	H 1.65 μm (Jy)	K_s 2.17 μm (Jy)
Tol 89	0.066	7.57 ± 1.05	11.35 ± 1.57	0.078	0.070	0.050	0.060	0.081	0.067	0.054
NGC 5408	0.068	...	...	0.092[b]	0.11[b]	...	...	0.19	0.17	0.11
NGC 5474	0.011	24.35 ± 3.37	27.18 ± 3.76	0.13	0.17	0.18	0.22	0.14	0.16	0.11
NGC 5713	0.039	5.16 ± 0.71	10.02 ± 1.39	0.11	0.14	0.16	0.20	0.37	0.39	0.33
NGC 5866	0.013	0.65 ± 0.09	4.15 ± 0.57	0.48	0.59	0.60	0.73	1.31	1.49	1.26
IC 4710	0.089	...	...	0.10	0.12	0.091	...	0.11	0.10	0.078
NGC 6822	0.231	306.7 ± 42.5	401.9 ± 56.0	1.58	2.24	1.96	1.49	5.66	5.64	4.26
NGC 6946	0.342	221.2 ± 30.8	417.6 ± 58.2	2.82[b]	4.10	...	5.08	7.27	5.47	5.66
NGC 7331	0.091	15.59 ± 2.16	29.70 ± 4.11	0.54	0.94	1.09	1.62	2.85	3.36	2.82
NGC 7552	0.014	7.73 ± 1.07	15.15 ± 2.11	0.17	0.26	0.25	0.23	0.71	0.80	0.70
NGC 7793	0.019	124.0 ± 17.2	145.1 ± 20.1	0.75	0.92	0.84	0.71	1.68	1.70	1.31

NOTES.—See § 3 for corrections that have been applied to the data. The uncertainties include both statistical and systematic effects ($\lesssim$10% for the optical and near-infrared data). The 2MASS near-infrared data are from Jarret et al. (2003).

[a] The far-ultraviolet detector was turned off during the observation.

[b] Data from the RC3 catalog (de Vaucouleurs et al. 1991).

(Gil de Paz et al. 2007).[18] Table 2 lists the global fluxes that include an asymptotic extrapolation to the isophotal profiles. The extrapolations are typically small and result in asymptotic fluxes that are, on average, 14% larger than those obtained at the optical radius: $\langle f_{UV}(\mathrm{asymptotic})/f_{UV}(R_{25})\rangle = 1.14$ with a dispersion of 0.16 and 0.14 in the far- and near-ultraviolet, respectively. Foreground field stars and background galaxies were masked before flux extraction (see Gil de Paz et al. 2007). Some of the SINGS galaxies have not yet been observed with *GALEX*, but observations are soon planned (NGC 1377, NGC 3184, NGC 5033, and IC 4710), and a few only have near-ultraviolet observations because the far-ultraviolet detector was turned off at that time (see Table 2). Bright nearby stars make it unlikely that *GALEX* will obtain data for NGC 5408.

The uncertainties listed in Table 2 include the formal uncertainties from the weighted fits to the growth curves using the uncertainties of the individual points in the growth curves, in addition to absolute calibration uncertainties of $\sim$15% in both the far- and near-ultraviolet.

The average far-ultraviolet radiation field can be estimated from the far-ultraviolet fluxes and a beam size that characterizes the area from which the far-ultraviolet flux is emitted. In units of the local Milky Way field (1.6×10^{-3} ergs cm^{-2} s^{-1}), the average far-ultraviolet radiation field, uncorrected for extinction, can be expressed as

$$G_0 = 2.2 \times 10^3 \left[\frac{f_\nu(1528\ \text{Å})}{\mathrm{mJy}}\right]\left(\frac{\mathrm{arcsec}}{\theta_{\mathrm{FUV}}}\right)^2, \qquad (1)$$

where θ_{FUV} is the equivalent radius of the ellipse including half of the total far-ultraviolet light (see Tables 1 and 2). Typical values for the SINGS sample span $1 \lesssim G_0 \lesssim 25$ with a median value of $G_0 = 7.4$.

3.2. *Optical Data*

Although RC3 fluxes (de Vaucouleurs et al. 1991) in the B and V bands are available for a large portion of the SINGS sample, we pursued a *BVRI* imaging campaign for reasons of consis-

[18] A few SINGS sources are not in the *GALEX* Atlas of Nearby Galaxies, but the observing and data reduction procedures for these galaxies are the same as for the Atlas targets (e.g., M81 Dwarf A, NGC 3773, NGC 4254, NGC 4725, NGC 6882, and NGC 6946).

tency, sensitivity, and completeness. The optical imaging for the SINGS project was carried out over the course of five observing runs at the Kitt Peak National Observatory (KPNO) 2.1 m telescope and one observing run at the Cerro Tololo Inter-American Observatory (CTIO) 1.5 m telescope between 2001 March and 2003 February. Broadband photometry was obtained in (Harris) *BVRI* using 2K × 2K CCDs with pixel scales and fields of view of 0.305″ and 10′ at KPNO and 0.433″ and 14.5′ at CTIO. Galaxies more extended than the CCD fields of view were imaged at multiple, overlapping pointings. Typical exposure times were 1440 s (B), 720 s (V), 420 s (R), and 840 s (I), usually split into two separate exposures to aid cosmic-ray removal. Such exposures reach a depth of about 25 mag arcsec^{-2} at a signal-to-noise ratio of $\sim$10 per resolution element.

Data processing consisted of standard routines such as bias subtraction, flat-fielding with both dome and twilight flats, cosmic-ray removal, and the mosaicking of overlapping pointings for galaxies with large angular extents. The southern 3′ of the KPNO 2.1 m CCD field of view suffers from vignetting; care is taken to remove as much of the vignetted portion of the KPNO images as feasible. Photometric standard stars were observed during each observing run to flux-calibrate the images. The images have photometric accuracy of 5% or better.

Global optical fluxes are extracted using the same apertures used for the IRAC and MIPS global flux extractions; these apertures cover at least the entire optical disk (see Table 1) and are chosen to be large enough to encompass all of the optical and infrared emission; in many instances the extended 160 μm emission drives the final choice of aperture. Sky estimation and subtraction are carried out through the use of multiple sky apertures placed near the source without overlapping the faintest isophotes visible from the galaxy. Foreground stars are edited from the optical images after first being conservatively identified using $f_\nu(3.6\ \mu\mathrm{m})/f_\nu(8.0\ \mu\mathrm{m})$ and $f_\nu(8.0\ \mu\mathrm{m})/f_\nu(24\ \mu\mathrm{m})$ color images [e.g., $f_\nu(8.0\ \mu\mathrm{m})/f_\nu(24\ \mu\mathrm{m}) > 8$ for stars].

3.3. *Infrared Data*

A full description of the infrared (2MASS, *ISO*, *IRAS*, *Spitzer*) and submillimeter (SCUBA) data can be found in Dale et al. (2005). In this section we present details of a few additional modifications and updates to the *Spitzer* data. For example, the MIPS flux calibrations and their uncertainties have been altered since Dale et al. (2005): the 24, 70, and 160 μm calibration factors have

TABLE 3
INFRARED, SUBMILLIMETER, AND RADIO FLUX DENSITIES

Galaxy	3.6 μm (Jy)	4.5 μm (Jy)	5.8 μm (Jy)	8.0 μm (Jy)	24 μm (Jy)	70 μm (Jy)	160 μm (Jy)	450 μm (Jy)	850 μm (Jy)	20 cm (mJy)
NGC 0024	0.10 ± 0.01	0.071 ± 0.01	0.089 ± 0.01	0.13 ± 0.02	0.14 ± 0.007	2.37 ± 0.19	8.19 ± 1.05	...	...	...
NGC 0337	0.097 ± 0.01	0.067 ± 0.009	0.14 ± 0.02	0.38 ± 0.05	0.68 ± 0.03	11.16 ± 0.79	20.09 ± 2.44	...	0.35 ± 0.05	110 ± 11
NGC 0584	0.37 ± 0.05	0.22 ± 0.03	0.18 ± 0.02	0.11 ± 0.01	0.048 ± 0.002	0.18 ± 0.05	1.18 ± 0.30[a]	...	...	<50
NGC 0628	0.87 ± 0.12	0.54 ± 0.08	1.16 ± 0.15	2.70 ± 0.34	3.19 ± 0.13	34.78 ± 2.50	126.2 ± 15.2	...	...	173 ± 17
NGC 0855	0.043 ± 0.006	0.028 ± 0.004	0.019 ± 0.003	0.046 ± 0.006	0.087 ± 0.004	1.70 ± 0.14	2.50 ± 0.36	...	...	4.9 ± 0.5
NGC 0925	0.31 ± 0.04	0.21 ± 0.03	0.35 ± 0.04	0.61 ± 0.08	0.95 ± 0.04	14.40 ± 1.04	43.33 ± 5.26	...	...	46 ± 5
NGC 1097	1.24 ± 0.17	0.80 ± 0.11	1.46 ± 0.18	3.19 ± 0.40	6.63 ± 0.27	59.84 ± 4.66	153.8 ± 18.5	...	1.44 ± 0.78	415 ± 42
NGC 1266	0.055 ± 0.008	0.042 ± 0.006	0.057 ± 0.008	0.090 ± 0.012	0.88 ± 0.04	12.69 ± 0.95	10.30 ± 1.29	...	...	116 ± 12
NGC 1291	2.11 ± 0.29	1.27 ± 0.17	0.96 ± 0.12	0.64 ± 0.08	0.57 ± 0.02	6.29 ± 0.46	28.60 ± 3.49	...	...	...
NGC 1316	2.48 ± 0.34	1.53 ± 0.21	1.13 ± 0.14	0.55 ± 0.07	0.43 ± 0.02	5.44 ± 0.40	12.61 ± 1.78	...	...	256 ± 26
NGC 1377	0.057 ± 0.008	0.085 ± 0.012	0.27 ± 0.04	0.42 ± 0.05	1.83 ± 0.08	6.35 ± 0.47	3.38 ± 0.42	...	...	<1.0
NGC 1404	0.73 ± 0.10	0.43 ± 0.06	0.33 ± 0.04	0.16 ± 0.02	0.088 ± 0.004	0.17 ± 0.12[a]	0.29 ± 0.28[a]	...	...	3.9 ± 0.6
NGC 1482	0.21 ± 0.03	0.15 ± 0.02	0.59 ± 0.08	1.56 ± 0.19	3.69 ± 0.15	32.45 ± 2.88	38.79 ± 4.69	...	0.33 ± 0.05	239 ± 24
NGC 1512	0.39 ± 0.05	0.24 ± 0.03	0.27 ± 0.03	0.44 ± 0.05	0.46 ± 0.02	6.65 ± 0.48	23.70 ± 2.86	...	...	7.0 ± 1
NGC 1566	0.75 ± 0.10	0.48 ± 0.07	0.91 ± 0.12	2.11 ± 0.26	2.83 ± 0.13	34.32 ± 2.51	102.1 ± 12.3	...	...	400 ± 40
NGC 1705	0.026 ± 0.004	0.018 ± 0.003	0.010 ± 0.002	0.017 ± 0.002	0.056 ± 0.002	1.38 ± 0.10	1.66 ± 0.21	...	...	...
NGC 2403	1.88 ± 0.25	1.31 ± 0.18	2.13 ± 0.27	4.11 ± 0.51	5.84 ± 0.24	86.36 ± 6.18	245.6 ± 29.6	...	...	330 ± 33
Holmberg II	0.071 ± 0.010	0.057 ± 0.008	0.031 ± 0.005	0.024 ± 0.005	0.20 ± 0.008	3.67 ± 0.26	4.46 ± 0.58	...	...	20 ± 3
M81 Dwarf A	0.002 ± 0.001	0.001 ± 0.001	<0.004	<0.002	<0.018	<0.17	<0.15	...	...	...
DDO 053	0.005 ± 0.001	0.004 ± 0.001	0.003 ± 0.001	0.007 ± 0.001	0.029 ± 0.001	0.40 ± 0.03	0.50 ± 0.11	...	...	...
NGC 2798	0.11 ± 0.02	0.081 ± 0.011	0.27 ± 0.03	0.63 ± 0.08	2.62 ± 0.11	21.72 ± 1.79	20.69 ± 2.50	...	0.19 ± 0.03	83 ± 9
NGC 2841	1.27 ± 0.17	0.75 ± 0.10	0.67 ± 0.09	1.16 ± 0.14	0.91 ± 0.04	10.22 ± 0.73	62.29 ± 7.54	...	...	84 ± 9
NGC 2915	0.054 ± 0.008	0.035 ± 0.005	0.033 ± 0.004	0.031 ± 0.004	0.063 ± 0.003	1.41 ± 0.11	1.46 ± 0.27	...	...	...
Holmberg I	0.012 ± 0.001	0.008 ± 0.001	0.007 ± 0.002	0.008 ± 0.002	0.013 ± 0.002	0.42 ± 0.08	0.90 ± 0.17	...	...	...
NGC 2976	0.43 ± 0.06	0.28 ± 0.04	0.51 ± 0.07	1.02 ± 0.13	1.37 ± 0.06	20.43 ± 1.45	52.56 ± 6.35	...	0.61 ± 0.24	51 ± 5
NGC 3049	0.040 ± 0.005	0.028 ± 0.004	0.065 ± 0.009	0.14 ± 0.02	0.43 ± 0.02	2.90 ± 0.21	4.86 ± 0.59	...	...	12 ± 2
NGC 3031	10.92 ± 1.48	6.53 ± 0.90	5.96 ± 0.75	8.04 ± 1.00	5.09 ± 0.20	85.18 ± 5.96	360.0 ± 43.4	...	...	380 ± 38
NGC 3034[b]	...	...	...	...	...	...	...	39.2 ± 9.8	5.51 ± 0.83	7660 ± 770
Holmberg IX	0.007 ± 0.001	0.004 ± 0.001	<0.013	<0.012	<0.037	<0.25	<0.48	...	...	...
M81 Dwarf B	0.005 ± 0.001	0.004 ± 0.001	0.003 ± 0.001	0.003 ± 0.001	0.009 ± 0.001	0.15 ± 0.03	0.39 ± 0.18	...	...	...
NGC 3190	0.37 ± 0.05	0.24 ± 0.03	0.25 ± 0.03	0.33 ± 0.04	0.27 ± 0.01	5.66 ± 0.40	15.01 ± 1.82	...	0.19 ± 0.04	43 ± 5
NGC 3184	0.56 ± 0.08	0.36 ± 0.05	0.67 ± 0.08	1.44 ± 0.18	1.43 ± 0.06	15.76 ± 1.12	70.48 ± 8.50	...	...	56 ± 5
NGC 3198	0.27 ± 0.04	0.17 ± 0.02	0.34 ± 0.04	0.68 ± 0.09	1.06 ± 0.04	10.27 ± 0.73	39.00 ± 4.93	...	...	27 ± 3
IC 2574	0.15 ± 0.02	0.091 ± 0.013	0.066 ± 0.009	0.066 ± 0.009	0.28 ± 0.01	5.55 ± 0.43	11.75 ± 1.50	...	...	11 ± 2
NGC 3265	0.028 ± 0.004	0.020 ± 0.003	0.041 ± 0.005	0.10 ± 0.01	0.30 ± 0.01	2.71 ± 0.20	2.70 ± 0.34	...	...	11 ± 2
Mrk 33	0.027 ± 0.004	0.019 ± 0.003	0.053 ± 0.007	0.13 ± 0.02	0.86 ± 0.04	4.35 ± 0.32	3.87 ± 0.48	...	0.04 ± 0.01	17 ± 2
NGC 3351	0.81 ± 0.11	0.51 ± 0.07	0.73 ± 0.09	1.33 ± 0.16	2.58 ± 0.12	24.18 ± 1.87	67.49 ± 8.28	...	...	44 ± 5
NGC 3521	2.05 ± 0.28	1.36 ± 0.19	2.56 ± 0.32	6.27 ± 0.76	5.51 ± 0.22	63.13 ± 4.54	222.3 ± 26.8	...	2.11 ± 0.82	357 ± 36
NGC 3621	0.99 ± 0.13	0.67 ± 0.09	1.62 ± 0.21	3.51 ± 0.44	3.70 ± 0.19	50.21 ± 3.94	139.0 ± 17.1	...	...	198 ± 20
NGC 3627	1.87 ± 0.25	1.25 ± 0.17	2.39 ± 0.30	5.58 ± 0.69	7.42 ± 0.30	92.63 ± 7.00	230.2 ± 27.7	...	1.86 ± 0.70	458 ± 46
NGC 3773	0.022 ± 0.003	0.014 ± 0.002	0.026 ± 0.004	0.048 ± 0.006	0.14 ± 0.006	1.58 ± 0.12	2.38 ± 0.33	...	...	5.8 ± 0.5
NGC 3938	0.32 ± 0.04	0.21 ± 0.03	0.41 ± 0.05	0.98 ± 0.12	1.09 ± 0.04	14.25 ± 1.01	51.98 ± 6.26	...	...	62 ± 7
NGC 4125	0.64 ± 0.09	0.37 ± 0.05	0.25 ± 0.03	0.14 ± 0.02	0.079 ± 0.004	1.11 ± 0.10	1.77 ± 0.28	...	...	<50
NGC 4236	0.25 ± 0.03	0.21 ± 0.03	0.11 ± 0.01	0.22 ± 0.03	0.55 ± 0.02	8.27 ± 0.59	20.43 ± 2.52	...	...	28 ± 3
NGC 4254	0.70 ± 0.10	0.47 ± 0.06	1.49 ± 0.19	3.94 ± 0.49	4.20 ± 0.17	50.29 ± 3.60	142.9 ± 17.2	...	1.01 ± 0.54	422 ± 42
NGC 4321	0.95 ± 0.13	0.64 ± 0.09	1.22 ± 0.15	2.89 ± 0.36	3.34 ± 0.13	40.59 ± 2.90	139.6 ± 16.8	...	0.88 ± 0.49	340 ± 34
NGC 4450	0.53 ± 0.07	0.33 ± 0.04	0.26 ± 0.03	0.27 ± 0.03	0.21 ± 0.01	3.42 ± 0.29	16.94 ± 2.14	...	...	9.4 ± 1

TABLE 3—*Continued*

Galaxy	3.6 μm (Jy)	4.5 μm (Jy)	5.8 μm (Jy)	8.0 μm (Jy)	24 μm (Jy)	70 μm (Jy)	160 μm (Jy)	450 μm (Jy)	850 μm (Jy)	20 cm (mJy)
NGC 4536	0.40 ± 0.05	0.29 ± 0.04	0.62 ± 0.08	1.66 ± 0.21	3.46 ± 0.14	31.99 ± 2.49	58.09 ± 7.00	. . .	0.42 ± 0.11	194 ± 19
NGC 4552	0.83 ± 0.11	0.49 ± 0.07	0.32 ± 0.04	0.17 ± 0.02	0.094 ± 0.004	0.54 ± 0.11	1.42 ± 0.73	. . .	. . .	100 ± 3
NGC 4559	0.35 ± 0.05	0.23 ± 0.03	0.42 ± 0.05	0.84 ± 0.10	1.12 ± 0.05	16.89 ± 1.20	54.15 ± 6.53	. . .	. . .	65 ± 7
NGC 4569	0.76 ± 0.10	0.47 ± 0.06	0.59 ± 0.08	1.02 ± 0.13	1.44 ± 0.06	12.37 ± 0.88	41.21 ± 5.17	. . .	0.47 ± 0.08	83 ± 9
NGC 4579	0.87 ± 0.12	0.52 ± 0.07	0.54 ± 0.07	0.73 ± 0.09	0.76 ± 0.03	9.53 ± 0.75	41.03 ± 4.95	. . .	0.44 ± 0.07	98 ± 10
NGC 4594	3.94 ± 0.53	2.31 ± 0.32	1.75 ± 0.22	1.30 ± 0.16	0.71 ± 0.04	8.02 ± 0.68	42.12 ± 5.58	. . .	0.37 ± 0.11	137 ± 14
NGC 4625	0.049 ± 0.006	0.030 ± 0.004	0.059 ± 0.008	0.13 ± 0.02	0.13 ± 0.006	2.06 ± 0.16	5.42 ± 0.68	. . .	. . .	7.1 ± 2
NGC 4631	1.26 ± 0.17	0.84 ± 0.11	2.49 ± 0.31	5.86 ± 0.73	8.15 ± 0.33	130.2 ± 9.9	289.5 ± 34.9	30.7 ± 10.0	5.73 ± 1.21	1200 ± 120
NGC 4725	1.14 ± 0.15	0.70 ± 0.10	0.75 ± 0.10	1.21 ± 0.15	0.86 ± 0.04	8.85 ± 0.66	59.91 ± 7.36	. . .	. . .	28 ± 3
NGC 4736	3.60 ± 0.49	2.32 ± 0.32	2.76 ± 0.35	5.17 ± 0.64	5.65 ± 0.23	93.93 ± 7.34	177.4 ± 21.4	. . .	1.54 ± 0.66	271 ± 27
DDO 154	0.004 ± 0.001	0.003 ± 0.001	<0.006	<0.004	0.008 ± 0.001[a]	0.065 ± 0.05[a]	0.35 ± 0.12[a]	. . .	. . .	. . .
NGC 4826	2.52 ± 0.34	1.57 ± 0.22	1.66 ± 0.21	2.35 ± 0.29	2.72 ± 0.15	55.16 ± 5.05	98.82 ± 12.67	. . .	1.23 ± 0.31	101 ± 10
DDO 165	0.016 ± 0.002	0.012 ± 0.002	0.005 ± 0.002	0.004 ± 0.001[a]	0.014 ± 0.001[a]	0.15 ± 0.07[a]	0.33 ± 0.26[a]	. . .	. . .	. . .
NGC 5033	0.64 ± 0.09	0.47 ± 0.06	0.82 ± 0.10	1.92 ± 0.24	1.97 ± 0.08	28.81 ± 2.09	91.07 ± 11.2	. . .	1.10 ± 0.55	178 ± 18
NGC 5055	2.38 ± 0.32	1.55 ± 0.21	2.67 ± 0.34	5.64 ± 0.70	5.73 ± 0.23	72.57 ± 5.16	302.3 ± 36.6	. . .	. . .	390 ± 39
NGC 5194	2.66 ± 0.36	1.80 ± 0.25	4.29 ± 0.54	10.64 ± 1.32	12.67 ± 0.53	147.1 ± 10.6	494.7 ± 59.8	. . .	2.61 ± 0.39	1490 ± 150
NGC 5195	0.83 ± 0.11	0.51 ± 0.07	0.47 ± 0.06	0.65 ± 0.08	1.40 ± 0.27	16.31 ± 3.26	14.86 ± 2.97	. . .	0.26 ± 0.04	50 ± 5
Tol 89	0.038 ± 0.005	0.025 ± 0.004	0.014 ± 0.002	0.059 ± 0.008	0.28 ± 0.01	2.03 ± 0.16	3.52 ± 0.51	. . .	. . .	4.2 ± 0.8
NGC 5408	0.052 ± 0.007	0.037 ± 0.005	0.041 ± 0.005	0.038 ± 0.005	0.43 ± 0.02	3.59 ± 0.27	2.57 ± 0.38	. . .	. . .	. . .
NGC 5474	0.10 ± 0.01	0.073 ± 0.010	0.077 ± 0.010	0.12 ± 0.01	0.18 ± 0.008	3.73 ± 0.27	10.56 ± 1.29	. . .	. . .	12 ± 2
NGC 5713	0.20 ± 0.03	0.14 ± 0.02	0.30 ± 0.04	1.16 ± 0.15	2.35 ± 0.10	23.69 ± 1.84	39.66 ± 4.79	. . .	0.57 ± 0.12	160 ± 16
NGC 5866	0.66 ± 0.09	0.42 ± 0.06	0.31 ± 0.04	0.31 ± 0.04	0.21 ± 0.009	8.71 ± 0.63	17.74 ± 2.14	0.8 ± 0.2	0.14 ± 0.02	23 ± 3
IC 4710	0.070 ± 0.010	0.047 ± 0.007	0.045 ± 0.006	0.065 ± 0.008	0.12 ± 0.005	2.37 ± 0.18	3.57 ± 0.48	. . .	. . .	. . .
NGC 6822	2.12 ± 0.29	1.38 ± 0.19	1.45 ± 0.18	1.41 ± 0.18	3.18 ± 0.13	63.75 ± 4.50	143.5 ± 17.4	. . .	. . .	69 ± 14
NGC 6946	3.31 ± 0.45	2.18 ± 0.30	5.88 ± 0.74	14.12 ± 1.76	20.37 ± 0.81	207.2 ± 16.1	502.8 ± 60.6	18.5 ± 4.6	2.98 ± 0.45	1395 ± 140
NGC 7331	1.61 ± 0.22	1.02 ± 0.14	1.87 ± 0.24	4.05 ± 0.50	4.36 ± 0.25	74.97 ± 6.62	189.5 ± 24.3	20.6 ± 8.1	2.11 ± 0.38	373 ± 37
NGC 7552	0.45 ± 0.06	0.36 ± 0.05	1.07 ± 0.14	2.71 ± 0.34	10.66 ± 0.44[c]	67.59 ± 11.1 [c]	93.39 ± 11.25	. . .	0.80 ± 0.17	276 ± 28
NGC 7793	0.77 ± 0.10	0.47 ± 0.06	1.04 ± 0.13	1.85 ± 0.23	2.05 ± 0.08	34.29 ± 2.43	126.2 ± 15.3	. . .	. . .	103 ± 10

NOTES.—See § 3 for details on the data. Upper limits (3 σ) are provided for nondetections.

[a] Possibly severely contaminated by background source(s).

[b] The bright core of NGC 3034 (M82) has rendered the *Spitzer* data extremely difficult to process. Saturation effects severely limit our ability to extract reliable global flux densities.

[c] Flux artificially low due to saturation effects.

TABLE 4
IRAC Aperture Correction Parameters

λ	A	B	C
3.5 μm..................................	0.82	0.370	0.910
4.5 μm..................................	1.00	0.380	0.940
5.8 μm..................................	1.49	0.207	0.720
8.0 μm..................................	1.37	0.330	0.740

Note.—See § 3 and http://spider.ipac.caltech.edu/staff/jarrett/irac/.

been respectively boosted by factors of 1.018, 1.107, and 1.049, and their systematic uncertainties have dropped to 4%, 7%, and 12% (C. W. Engelbracht et al. 2007, in preparation; K. D. Gordon et al. 2007, in preparation; J. Stansberry et al. 2007, in preparation). The uncertainties provided in Table 3 include both calibration and statistical uncertainties. Calibration uncertainties are 5%–10% for IRAC 3.6 and 4.5 μm data and 10%–15% for IRAC 5.8 and 8.0 μm data; 10% calibration uncertainties are used in Table 3.

The IRAC flux densities in Table 3 include extended source aperture corrections provided by the *Spitzer* Science Center.[19] These corrections account for the "extended" emission due to the wings of the point-spread function (PSF) and also for the scattering of the diffuse emission across the IRAC focal plane. For an effective aperture radius $r = (ab)^{1/2}$ in arcseconds derived from the semimajor a and semiminor b ellipse axes provided in Table 1, the IRAC extended source aperture correction is

$$f_{\text{true}}^{\text{IRAC}}/f_{\text{measured}}^{\text{IRAC}} = Ae^{-r^B} + C, \qquad (2)$$

where A, B, and C are listed in Table 4. The average extended source aperture corrections (~10% uncertain) for the SINGS IRAC photometry are [0.912, 0.942, 0.805, 0.749] at [3.6, 4.5, 5.8, 8.0] μm.

The MIPS flux densities in Table 3 also include extended source aperture corrections. Three high-resolution models of a galaxy's structure are generated by convolving an R-band image of the galaxy with the MIPS PSFs. The MIPS aperture corrections listed in Table 5 are computed for the same apertures used in the global flux extractions (Table 1). The median aperture corrections are [1.01, 1.04, 1.10] at [24, 70, 160] μm. The uncertainties in the aperture corrections are typically a few percent and are based on the differences between the canonical and "minimum" corrections. Minimum MIPS aperture corrections are computed assuming point-source light distributions.

Finally, a correction for 70 μm nonlinearity effects is included in this presentation. A preliminary correction of the form

$$f_{\text{true}}^{70\,\mu\text{m}} = 0.581 \left(f_{\text{measured}}^{70\,\mu\text{m}}\right)^{1.13}, \qquad (3)$$

derived from data presented by K. D. Gordon et al. (2007, in preparation), is applied to pixel values above a threshold of ~66 MJy sr^{-1}. A small fraction of the pixels in a total of 40 SINGS 70 μm images require such a correction. The median correction to the global 70 μm flux density for these 40 galaxies is a factor of 1.03, with the three largest corrections being factors of 1.124 (NGC 4826), 1.128 (NGC 1482), and 1.158 (NGC 7552).

3.4. Radio Data

Global 20 cm continuum fluxes from the literature are available for 62 SINGS galaxies, with data for 51 of these galaxies

[19] See http://spider.ipac.caltech.edu/staff/jarrett/irac/.

TABLE 5
Infrared and Submillimeter Aperture Correction Factors

Galaxy	24 μm	70 μm	160 μm	450 μm	850 μm
NGC 0024..................	1.06	1.10	1.20	. . .	. . .
NGC 0337..................	1.01	1.06	1.15	. . .	. . .
NGC 0584..................	1.00	1.04	1.11	. . .	. . .
NGC 0628..................	1.02	1.03	1.06	. . .	. . .
NGC 0855..................	1.02	1.07	1.15	. . .	. . .
NGC 0925..................	1.03	1.04	1.07	. . .	. . .
NGC 1097..................	1.01	1.02	1.06	. . .	2.09
NGC 1266..................	1.01	1.05	1.13	. . .	. . .
NGC 1291..................	1.01	1.02	1.04	. . .	. . .
NGC 1316..................	1.06	1.02	1.18	. . .	. . .
NGC 1377..................	1.02	1.06	1.15	. . .	. . .
NGC 1404..................	1.00	1.02	1.07	. . .	. . .
NGC 1482..................	1.00	1.03	1.10	. . .	. . .
NGC 1512..................	1.04	1.05	1.06	. . .	. . .
NGC 1566..................	1.04	1.05	1.04	. . .	. . .
NGC 1705..................	1.04	1.12	1.19	. . .	. . .
NGC 2403..................	1.00	1.00	1.02	. . .	. . .
Holmberg II..............	1.00	1.02	1.09	. . .	. . .
M81 Dwarf A	1.00	1.00	1.00	. . .	. . .
DDO 053..................	1.03	1.15	1.48	. . .	. . .
NGC 2798..................	1.03	1.08	1.19	. . .	1.08
NGC 2841..................	1.01	1.04	1.10	. . .	. . .
NGC 2915..................	1.07	1.15	1.33	. . .	. . .
Holmberg I................	1.01	1.05	1.15	. . .	. . .
NGC 2976..................	1.00	1.03	1.10	. . .	1.56
NGC 3049..................	1.02	1.07	1.18	. . .	. . .
NGC 3031..................	1.00	1.00	1.01	. . .	. . .
NGC 3034..................	1.00	1.00	1.00	. . .	. . .
Holmberg IX.............	1.00	1.00	1.00	. . .	. . .
M81 Dwarf B............	1.12	1.16	1.86	. . .	. . .
NGC 3190..................	1.01	1.05	1.13	. . .	1.12
NGC 3184..................	1.00	1.00	1.05	. . .	. . .
NGC 3198..................	1.00	1.02	1.08	. . .	. . .
IC 2574	1.04	1.07	1.12	. . .	. . .
NGC 3265..................	1.02	1.07	1.16	. . .	. . .
Mrk 33	1.02	1.07	1.16	. . .	. . .
NGC 3351..................	1.04	1.06	1.11	. . .	. . .
NGC 3521..................	1.00	1.01	1.05	. . .	1.56
NGC 3621..................	1.06	1.07	1.09	. . .	. . .
NGC 3627..................	1.00	1.01	1.06	. . .	1.53
NGC 3773..................	1.07	1.13	1.15	. . .	. . .
NGC 3938..................	1.01	1.03	1.08	. . .	. . .
NGC 4125..................	1.09	1.16	1.31	. . .	. . .
NGC 4236..................	1.00	1.02	1.06	. . .	. . .
NGC 4254..................	1.00	1.02	1.07	. . .	2.06
NGC 4321..................	1.00	1.01	1.06	. . .	2.19
NGC 4450..................	1.04	1.08	1.16	. . .	. . .
NGC 4536..................	1.00	1.02	1.08	. . .	1.30
NGC 4552..................	1.00	1.03	1.11	. . .	. . .
NGC 4559..................	1.00	1.03	1.09	. . .	. . .
NGC 4569..................	1.00	1.01	1.07	. . .	1.11
NGC 4579..................	1.01	1.04	1.07	. . .	. . .
NGC 4594..................	1.06	1.09	1.17	. . .	1.33
NGC 4625..................	1.01	1.06	1.16	. . .	. . .
NGC 4631..................	1.00	1.00	1.05	1.27	1.17
NGC 4725..................	1.03	1.05	1.10	. . .	. . .
NGC 4736..................	1.00	1.00	1.02	. . .	1.67
DDO 154...................	1.06	1.14	1.35	. . .	. . .
NGC 4826..................	1.08	1.09	1.14	. . .	1.24
DDO 165...................	1.02	1.09	1.24	. . .	. . .
NGC 5033..................	1.00	1.01	1.05	. . .	1.93
NGC 5055..................	1.00	1.00	1.03	. . .	. . .
NGC 5194..................	1.00	1.00	1.01	. . .	. . .
NGC 5195..................	1.01	1.06	1.13	. . .	. . .
Tol 89........................	1.08	1.14	1.22	. . .	. . .

TABLE 5—*Continued*

Galaxy	24 μm	70 μm	160 μm	450 μm	850 μm
NGC 5408..................	1.01	1.05	1.12	. . .	. . .
NGC 5474..................	1.00	1.03	1.09	. . .	. . .
NGC 5713..................	1.01	1.06	1.14	. . .	1.17
NGC 5866..................	1.00	1.03	1.09	. . .	. . .
IC 4710	1.03	1.08	1.19	. . .	. . .
NGC 6822..................	1.00	1.00	1.01	. . .	. . .
NGC 6946..................	1.00	1.00	1.03	. . .	. . .
NGC 7331..................	1.08	1.10	1.16	1.44	1.11
NGC 7552..................	1.01	1.02	1.13	. . .	1.17
NGC 7793..................	1.01	1.03	1.08	. . .	. . .

Notes.—IRAC aperture corrections are described by eq. (2). See § 3.3 and Dale et al. (2005) for details.

taken from the New VLA Sky Survey catalog (Condon et al. 1998; Yun et al. 2001; see Table 3). Although this is a snapshot survey and prone to miss extended emission from galaxies having large angular extents, proper attention has been paid to these effects to derive unbiased 1.4 GHz fluxes (e.g., Yun et al. 2001). The 20 cm data for 11 additional galaxies were taken from Condon

(1987), Hummel (1980), Condon et al. (1990), Wright & Otrupcek (1990), Bauer et al. (2000), and Cannon et al. (2006b).

4. RESULTS

4.1. *Global Broadband Spectral Energy Distributions*

Figure 1 shows the ultraviolet-to-submillimeter SEDs for the SINGS sample. The solid line is the sum of a dust (*dashed line*) and a stellar (*dotted line*) model. The dust curve is a Dale & Helou (2002) model (least squares) fitted to ratios of the 24, 70, and 160 μm fluxes (a dust curve for NGC 3034 is fitted using *IRAS* 25, 60, and 100 μm data, since the MIPS data for this galaxy are saturated). The α_{SED} listed within each panel parameterizes the distribution of dust mass as a function of heating intensity, as described in Dale & Helou (2002). Broadly speaking, smaller values of α_{SED} (more heating from stronger interstellar radiation fields) correspond to later Hubble types and larger infrared-to-ultraviolet ratios. The stellar curve is a 1 Gyr continuous star formation, solar metallicity curve from Vazquez & Leitherer (2005) fitted to the 2MASS data. The initial mass function for this curve utilizes a double power-law form, with $\alpha_{1,IMF} = 1.3$ for $0.1 < m/M_\odot < 0.5$ and $\alpha_{2,IMF} = 2.3$ for $0.5 < m/M_\odot < 100$ (e.g.,
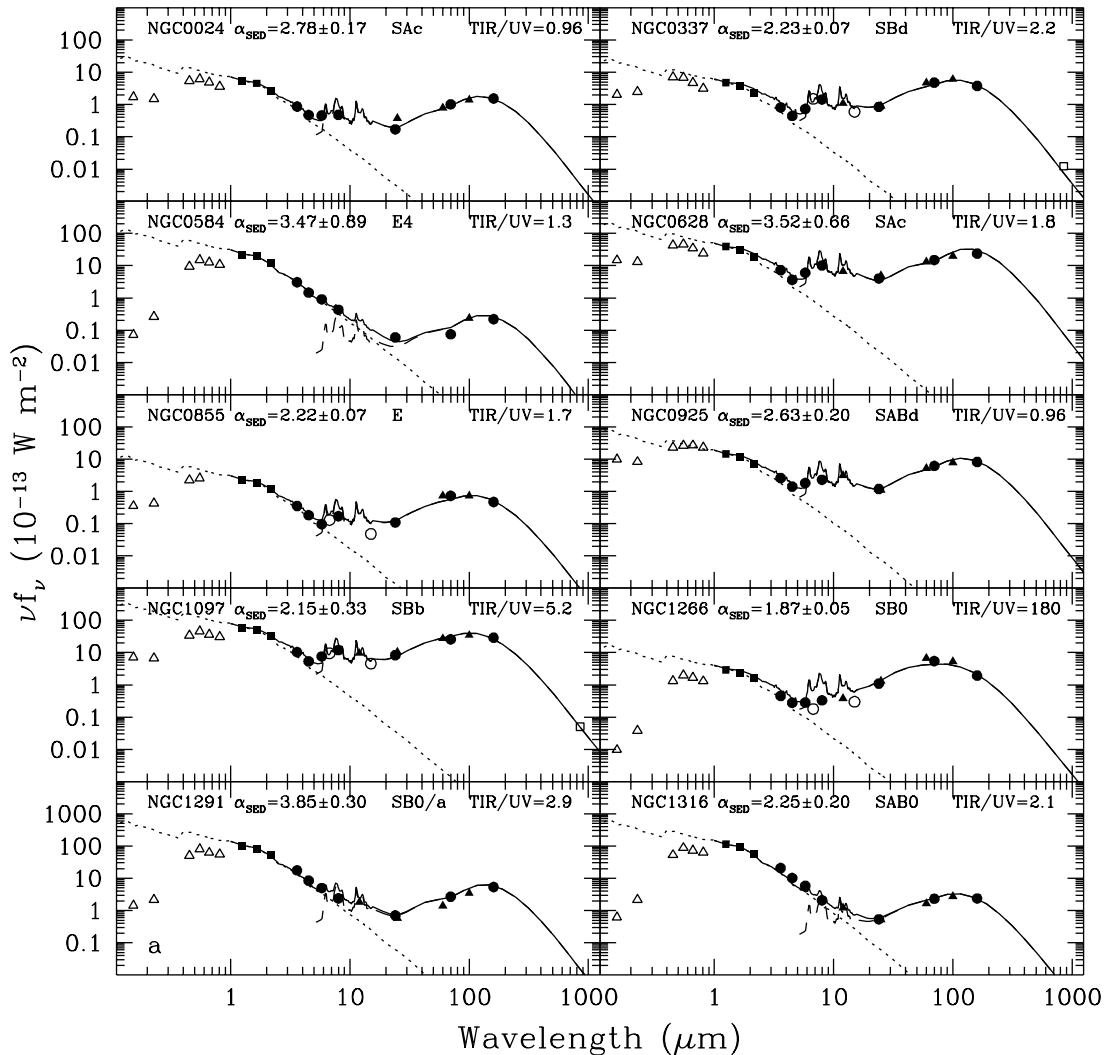
Fig. 1.—Globally integrated 0.15−850 μm SEDs for the SINGS sample. *GALEX* and optical, 2MASS, *Spitzer*, *IRAS*, *ISO*, and SCUBA data are represented by open triangles, filled squares, filled circles, filled triangles, open circles, and open squares, respectively. The solid line is the sum of a dust (*dashed line*) and a stellar (*dotted line*) model. The dust curve is a Dale & Helou (2002) model fitted to ratios of the 24, 70, and 160 μm fluxes; the α_{SED} listed within each panel parameterizes the distribution of dust mass as a function of heating intensity, as described in Dale & Helou (2002). The stellar curve is a 1 Gyr continuous star formation, solar metallicity curve from Vazquez & Leitherer (2005) fitted to the 2MASS data (see § 4 for details). [*See the electronic edition of the Journal for a color version of this figure.*]
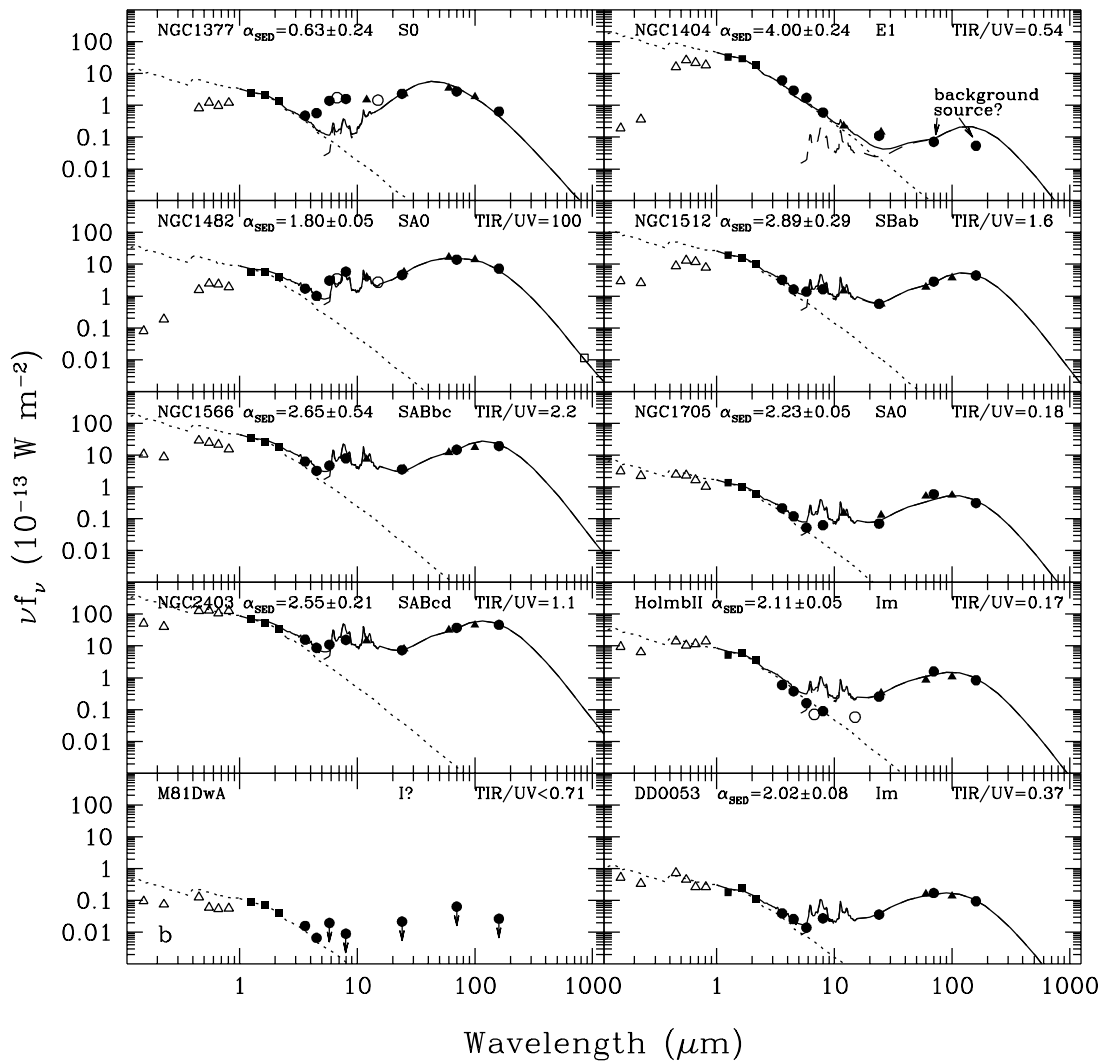
FIG. 1.—Continued

Kroupa 2002). Although this stellar curve (not adjusted for internal extinction) may not be applicable to many galaxies, especially elliptical galaxies, it is included as a "standard" reference against which deviations in the ultraviolet and optical can be compared from galaxy to galaxy. The stellar curve also serves to highlight the relative importance of stars and dust in each galaxy, particularly in the transition from stellar to dust emission in the mid-infrared (e.g., NGC 1404 vs. NGC 1482).

Several galaxies show mid-infrared data that deviate from the fits. Most of these systems are low-metallicity objects (e.g., Holmberg II, NGC 2915, IC 2574, DDO 154, DDO 165, and NGC 6822), objects that have been shown to be deficient in polycyclic aromatic hydrocarbon (PAH) emission (see the discussion in § 4.2). The mid-infrared data for NGC 1377 are also quite discrepant from the model, showing a strong excess for each of the broadband filters from 3.6 to 15 μm. The substantial hot dust emission and lack of optical signatures or synchrotron radiation led Roussel et al. (2003) to infer that this heavily extincted system is undergoing the very beginnings of an intense burst of star formation.

4.2. Spectral Energy Distributions Binned by the Infrared-to-Ultraviolet Ratio

Analysis of the distribution of global (spatially integrated) SEDs is a sensible starting point for current cosmology surveys

(e.g., Rowan-Robinson et al. 2005). Figure 2 shows a stack of SINGS SEDs that emphasizes the infrared-to-ultraviolet variations within the SINGS sample. Each SED in the stack represents an average of approximately 10 individual SEDs that fall within a given bin of the total infrared-to-ultraviolet ratio [TIR/(FUV+ NUV); the bins are indicated in the figure legend]. The ultraviolet emission for this ratio is computed as $\nu f_\nu(1500\ \text{Å}) + \nu f_\nu(2300\ \text{Å})$, whereas the "total infrared" is the dust continuum emission between 3 and 1100 μm (Dale et al. 2001), computed using the MIPS 24, 70, and 160 μm fluxes and equation (4) of Dale & Helou (2002). The spectra are arbitrarily normalized at the 2MASS K_s band wavelength.

Several features in the stack are immediately noticeable. The ultraviolet slopes vary from positive values for galaxies with high infrared-to-ultraviolet ratios to negative values for low infrared-to-ultraviolet ratio galaxies (as explored in detail in § 5.6). The 4000 Å break shows up quite clearly, even at this coarse spectral "resolution." Other obvious features include the broad far-infrared peak, signifying emission from cool to warm large grains; the contributions from PAHs appearing as mid-infrared emission features; the near-infrared hump arising from photospheric emission from old stellar populations; and a near-infrared H− opacity signature for high infrared-to-ultraviolet systems. Note also the broad spread in the ultraviolet data compared to that in the far-infrared. Since the
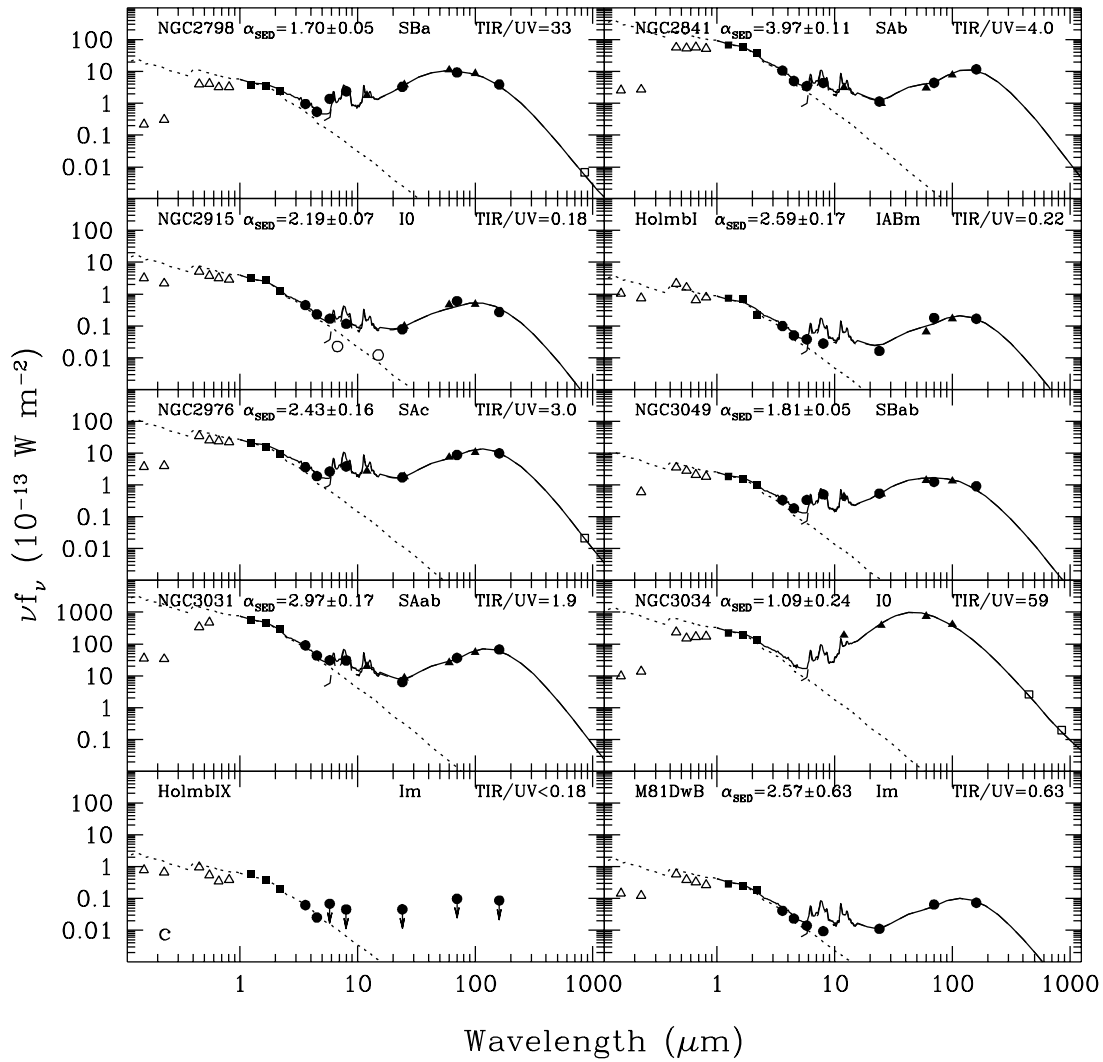
Fig. 1.—*Continued*

spectra are normalized at K_s, this difference implies that there is a larger spread in ultraviolet light per unit stellar mass than infrared light per unit stellar mass (Gil de Paz et al. [2007], for example, find that [FUV − K] spans 11 mag in their *GALEX* Atlas). The variations in the infrared-to-ultraviolet ratio studied later in this work are largely driven by variations in the ultraviolet emission.

Close inspection of Figure 2 reveals that most of the variation in the stacked spectra stems from the two extreme bins (bins "1" and "6") in the infrared-to-ultraviolet ratio. However, substantial variations are still seen in bins 2–5 at ultraviolet and mid-infrared wavelengths. The bin 2–5 range is 0.88, 0.78, 0.24, and 0.16 dex at 0.15, 0.23, 8.0, and 24 μm, respectively (compared to the bin 1–6 range of 1.76, 1.46, 0.80, and 0.80 dex at the same wavelengths). The spread at ultraviolet wavelengths is presumably significantly affected by variations in dust extinction. The range in 8.0 μm emission, on the other hand, is likely due to PAH destruction/formation variations. Low-metallicity systems, for example, are known to be deficient in PAH emission (e.g., Dale et al. 2005; Engelbracht et al. 2005; Galliano et al. 2005; Walter et al. 2006). Indeed, eight of the nine galaxies in the lowest infrared-to-ultraviolet ratio bin have low metallicities [12 + log (O/H) < 8.1; J. Moustakas et al. 2007, in preparation], and this bin's average spectrum in Figure 2 shows very low mid-infrared emission. The 24 μm emission from galaxies is known to be sensitive

to the star formation rate (e.g., Dale et al. 2005; Gordon et al. 2004; Helou et al. 2004; Hinz et al. 2004; Calzetti et al. 2005); the observed variations at this wavelength may be strongly affected by the range in the sample's star formation properties.

4.3. *Principal Component Analysis*

A principal component analysis can help to quantify relative contributions to the observed variations in a sample of SEDs (Deeming 1964). A set of i eigenvectors $\{e_i\}$ and their corresponding eigenvalues $\{e_i\}$ for our sample of N galaxies are computed from a diagonalization of the covariance matrix

$$C_{jk} = \frac{1}{N} \Sigma_{i=1}^{N} \nu f_\nu^i(\lambda_j) \nu f_\nu^i(\lambda_k), \qquad (4)$$

where $\nu f_\nu^i(\lambda_j)$ is the flux of the ith spectrum at wavelength λ_j. We restrict the computation of the covariance matrix to involve only those wavelengths for which we have a substantial database of fluxes; submillimeter data at 450 and 850 μm are not included in the principal component analysis. Furthermore, to avoid spurious results, we do not include in our analysis any SINGS galaxies without a secure detection/measurement at any of the ultraviolet, optical, near-infrared, or infrared wavelengths listed in
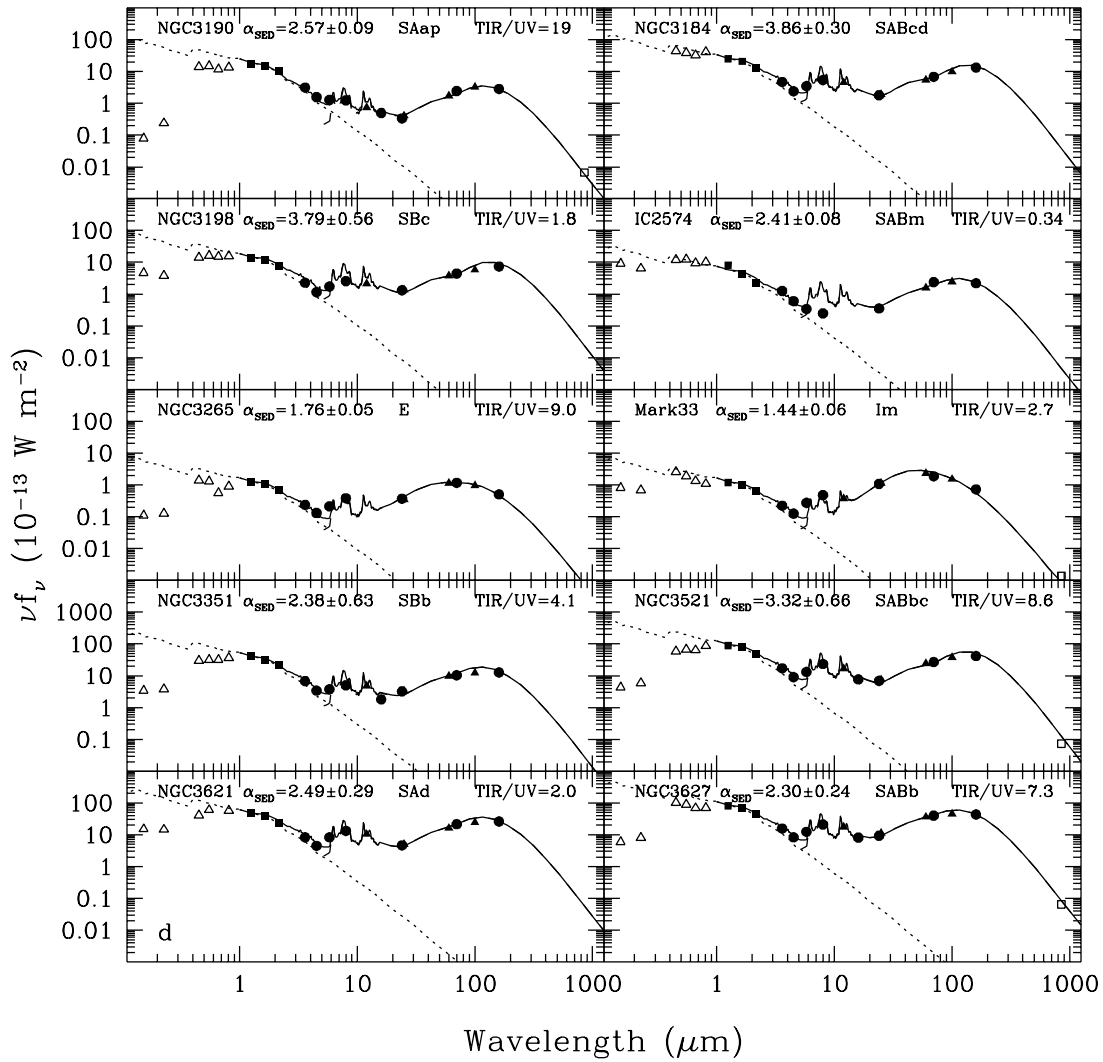
Fig. 1.—*Continued*

Tables 2 and 3. Hence, our principal component analysis involves only about three-fourths of the SINGS sample (Table 1 indicates which systems are involved). Our principal component analysis is carried out after normalizing the spectra at the 2MASS K_s band wavelength.

The principal component analysis has produced eigenvectors that describe different components of the sample spectra (Fig. 3). The most important eigenvectors are the first two. Eigenvector e_1 appears to describe the contribution of unobscured starlight (including starlight from star formation regions) to the galaxies' spectra. This eigenvector also includes additional low-level far-infrared emission that may represent cirrus emission from the diffuse interstellar medium. Eigenvector e_2 appears to describe the effects of dust on the shape of the spectrum. This eigenvector demonstrates that as the dust content of the galaxies increases, the mid- and far-infrared flux densities increase while the starlight becomes redder (i.e., the ultraviolet and blue light decreases while the red and near-infrared light increases).

The individual eigenvalues normalized by the sum $\Sigma_j e_j$ of all eigenvalues indicate the fractional contribution of each corresponding eigenvector to the variation in the spectral atlas (when normalized at K_s). The normalized e_1 and e_2 eigenvalues (which correspond to the e_1 and e_2 eigenvectors) are 0.88 and 0.07, respectively. In other words, e_1 and e_2 represent 88% and 7% of the

total variation in the spectral atlas. The remaining 5% of the variation is represented by additional eigenvectors with corresponding normalized eigenvalues that are individually 0.02 or smaller. To quantify the uncertainty on these numbers, we have performed 10,000 Monte Carlo simulations of the principal component analysis. For each simulation we use the tabulated flux uncertainties to add a random (Gaussian deviate) flux offset to every galaxy's flux at each wavelength. The means of the two largest normalized eigenvalues from these simulations are $\langle e_1 \rangle = 0.88 \pm 0.01$ and $\langle e_2 \rangle = 0.07 \pm 0.01$, with the error bars reflecting the standard deviations in the simulations. The eigenspectra and error bars in Figure 3 reflect the mean values and standard deviations in the simulations.

5. THE INFRARED-TO-ULTRAVIOLET RATIO

The infrared-to-ultraviolet ratio is a rough measure of the amount of extinction at ultraviolet wavelengths. The infrared-to-ultraviolet ratio in galaxies is also sensitive to the metal content, luminosity, star formation history, and the relative distribution of interstellar grains with respect to their heating sources. What is the predominant driver of the variations in this ratio in galaxies? Which parameters can be used to most easily quantify these variations, with the aim of simplifying SED analysis? Various possibilities are presented and discussed below.
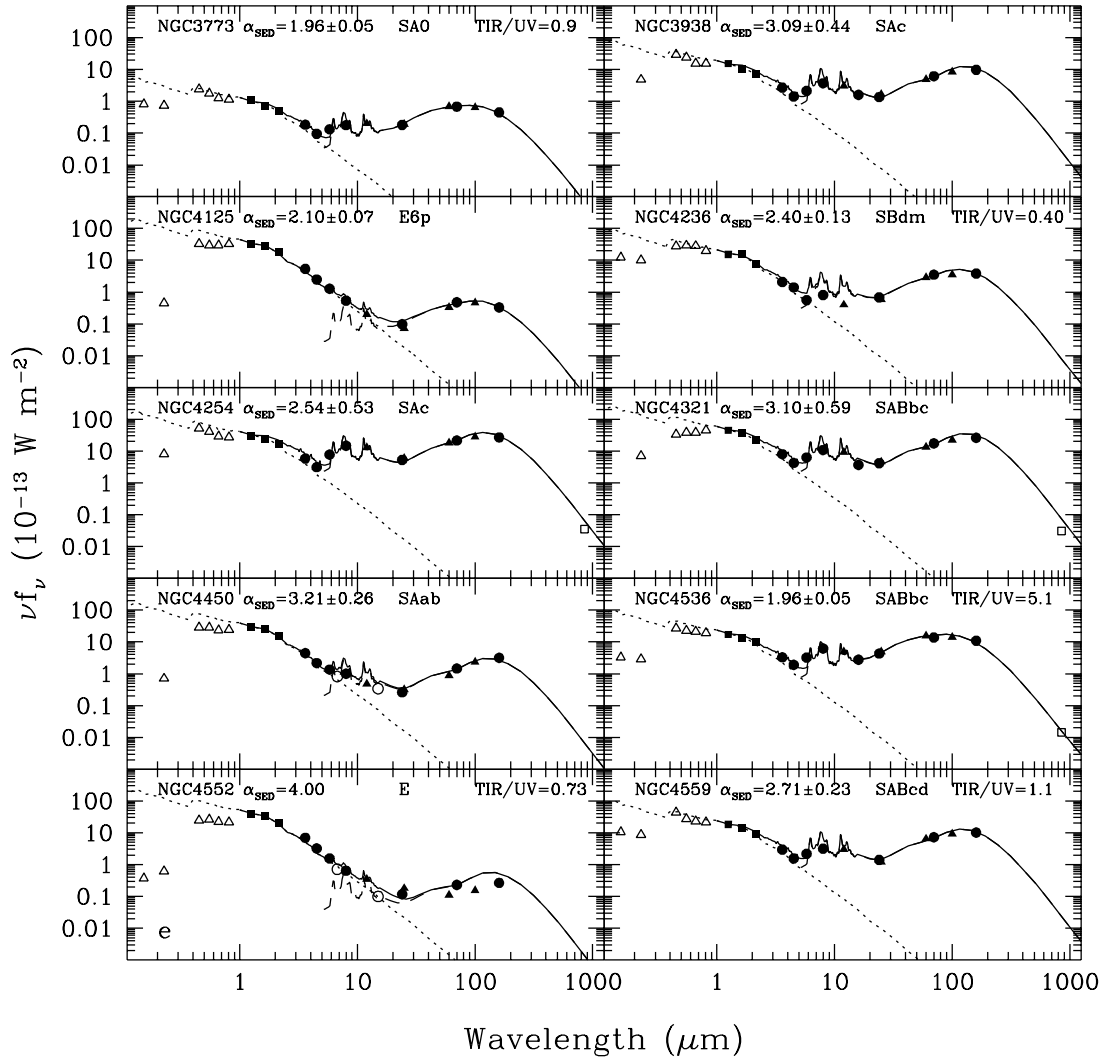
Fig. 1.—*Continued*

5.1. *Inclination*

The tilt of a spiral disk with respect to the observer's line of sight affects the observed intensity and colors (e.g., Bruzual et al. 1988; Boselli & Gavazzi 1994; Giovanelli et al. 1995; Kuchinski et al. 1998). The "disk" inclination can be computed from the observed semimajor and semiminor axes, a and b, assuming that disks are oblate spheroids with intrinsic axial ratio $(b/a)_{int}$ using the relation

$$\cos^2 i = \frac{(b/a)^2 - (b/a)_{int}^2}{1 - (b/a)_{int}^2}, \qquad (5)$$

where $(b/a)_{int} \simeq 0.2$ for morphological types earlier than Sbc and $(b/a)_{int} \simeq 0.13$ otherwise (see Dale et al. 1997 and references therein). Figure 4 gives the infrared-to-ultraviolet ratio as a function of galaxy disk inclination. Galaxies with elliptical and irregular morphologies have not been included in the plot. The dotted line (normalized to an infrared-to-ultraviolet ratio of unity at zero inclination) shows the expected effect of extinction on the ultraviolet data with changing inclination using the thin-disk model and a central face-on optical depth in the B band of $\tau_B^f = 2$ described in Tuffs et al. (2004). The ratio does not obviously trend with galaxy orientation; if there is a trend consistent with the

model of Tuffs et al. (2004), it is a weak trend that is washed out by a large dispersion. The data in Figure 4 indicate that moderate disk inclinations are not a dominant factor in determining the infrared-to-ultraviolet ratio in SINGS galaxies.

5.2. *Hubble Type*

Figure 5 displays the infrared-to-ultraviolet ratio as a function of galaxy optical morphology. In general, the ultraviolet light increases in importance and the dust emission decreases in importance as the morphology changes from early-type spiral galaxies to late-type spiral galaxies to irregular galaxies, reflecting the changing significance of recent star formation and dust content/distribution to the overall energy budget in galaxies (see also Buat & Xu 1996; Gil de Paz et al. 2007). One interpretation is that the infrared-to-ultraviolet ratio increases as the redder, older stellar populations increasingly dominate for earlier type spiral galaxies, but as shown in § 5.3, the increased porosity of star-forming regions for more actively star-forming galaxies may play a key role in this trend. Elliptical and S0 galaxies do not follow the general trend exhibited by the spiral and irregular galaxies; some elliptical and S0 galaxies show comparatively low infrared-to-ultraviolet ratios. This deviation to low infrared-to-ultraviolet ratios for some of the earliest type galaxies could be due to a relative paucity of dust grains intercepting ultraviolet/optical/near-infrared
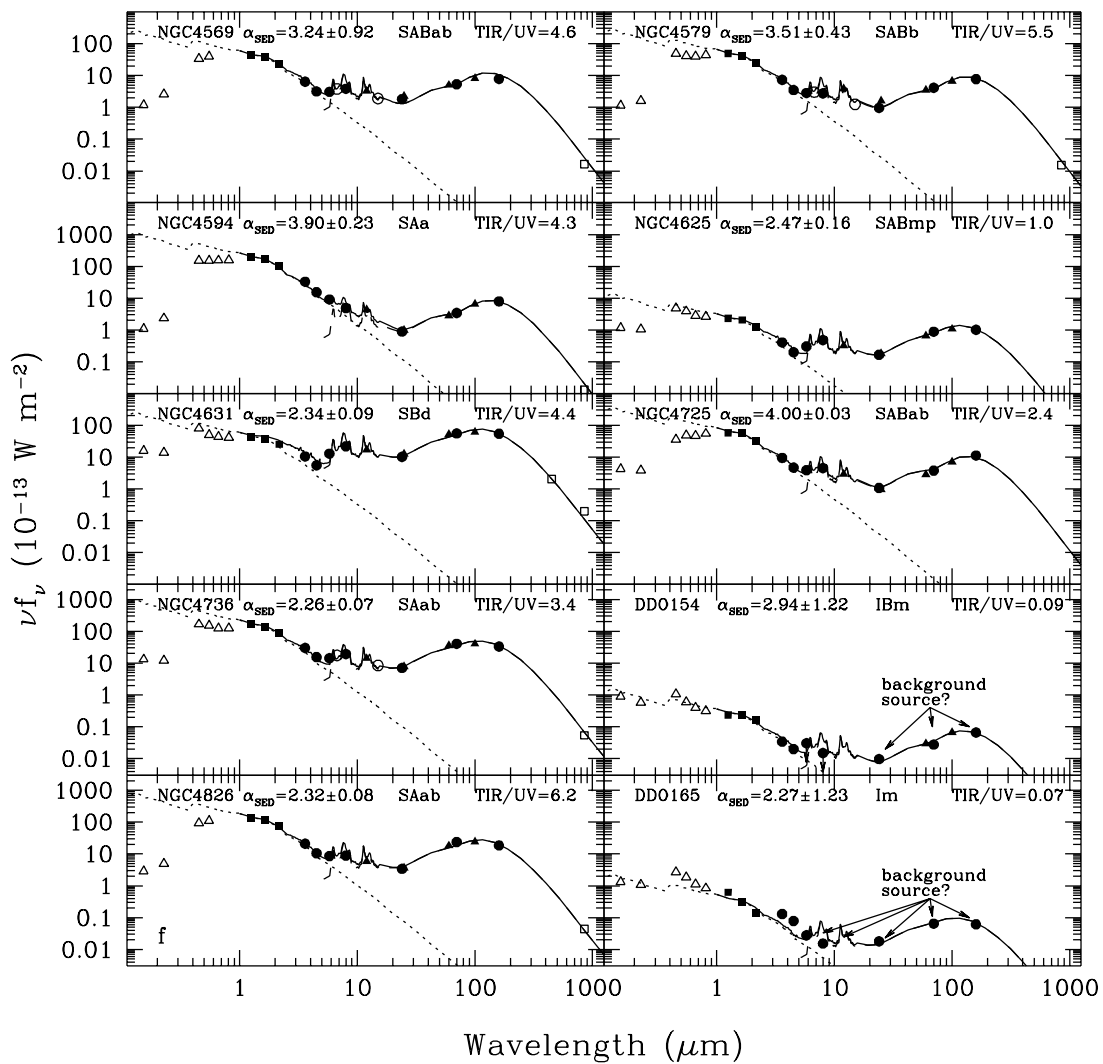
Fig. 1.—Continued

photons and reprocessing that energy into the infrared; the infrared portion of the bolometric luminosity in elliptical galaxies is typically only a few percent (Xilouris et al. 2004). Moreover, some elliptical systems are conspicuous ultraviolet emitters, with the emission thought to mainly arise from low-mass, helium-burning stars from the extreme horizontal branch and later phases of stellar evolution (for a review see O'Connell 1999). Low or moderate levels of star formation could also contribute to the ultraviolet emission in early-type galaxies (e.g., Fukugita et al. 2004). Recent evidence shows that strong ultraviolet emitters are the largest contributors to the significant scatter in the ultraviolet colors of early-type galaxies (e.g., Yi et al. 2005; Rich et al. 2005).

This wide range in the fractional ultraviolet luminosity also leads to significant scatter in the infrared-to-ultraviolet ratio. Although the statistics are based on small numbers, a similarly large dispersion is seen for irregular systems at the other end of the morphological spectrum. Part of this dispersion is likely associated with the metal content in irregular/dwarf systems. In general, irregular galaxies are quite blue and metal-poor (e.g., Hunter & Gallagher 1986; van Zee et al. 1997). Ultraviolet/optical continuum emission from low-metallicity galaxies experiences less extinction, which inhibits the production of infrared continuum emission (see previous paragraph). The combination of these effects leads to lower infrared-to-ultraviolet ratios in irregular galaxies.[20]

5.3. Far-Infrared Color

Although dwarf irregular galaxies show low infrared-to-ultraviolet ratios, their interstellar dust grains tend to be vigorously heated. The lower metallicity in these systems results in less line blanketing, which in turn leads to harder radiation fields. Many of the dwarf and irregular systems in the SINGS sample indeed have elevated $f_\nu(70\ \mu m)/f_\nu(160\ \mu m)$ ratios (e.g., Dale et al. 2005; Walter et al. 2006; see also Boselli et al. 2003), indicating strong overall heating of the dust grain population. The warmer far-infrared colors for SINGS dwarf/irregular galaxies are evident in Figure 6, which plots the infrared-to-ultraviolet ratio versus far-infrared color for the entire SINGS sample.

An interesting feature to this plot is the apparent wedge-shaped distribution, with a progressively smaller range in the infrared-to-ultraviolet ratio for cooler far-infrared colors. There is no obvious trend in infrared-to-ultraviolet ratio with disk inclination (Fig. 4), so it is unlikely that the distribution in Figure 6 is due solely to disk orientation.

[20] The amorphous, starbursting M82 hosts a large infrared-to-ultraviolet ratio and should be considered separately from the dwarf irregular galaxies.
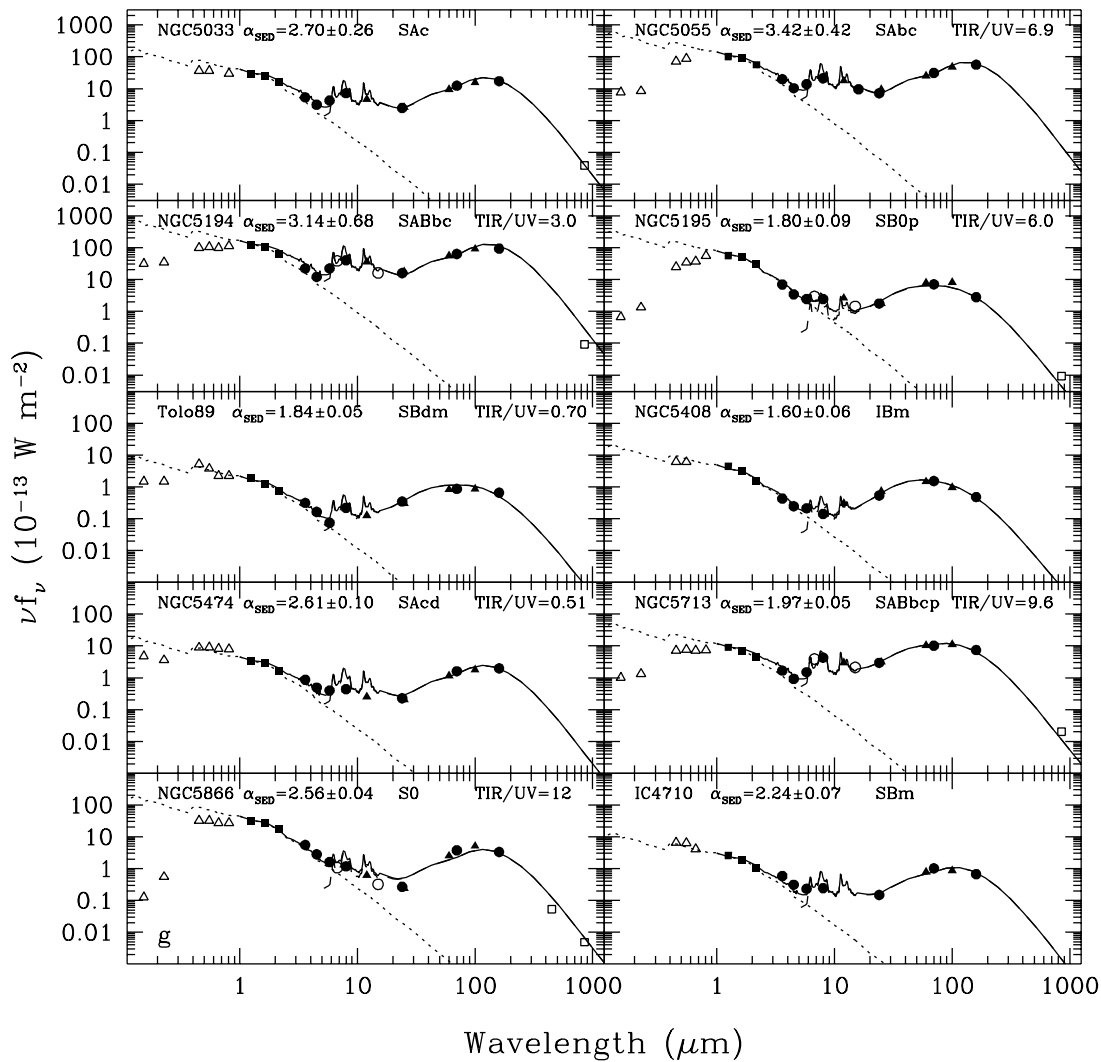
FIG. 1.—*Continued*

The small data points without error bars come from the (*IRAS* based) *GALEX* Atlas of Nearby Galaxies (Gil de Paz et al. 2007) and follow the same general distribution as the SINGS data, suggesting that this wedge-shaped distribution is unlikely a sample selection effect. Presumably the upper left portion of this figure, for example, is empty since a large infrared-to-ultraviolet ratio requires lots of dust opacity, but higher opacity implies a larger density of interstellar dust closer to heating sources, therefore leading to warm dust and high values of $f_\nu(70\ \mu m)/f_\nu(160\ \mu m)$.

The relative distribution of dust grains and their heating sources may, in fact, play a key role in creating this overall wedge-shaped distribution. As argued above, it is reasonable to assume that galaxies with relatively high $f_\nu(70\ \mu m)/f_\nu(160\ \mu m)$ ratios have hotter dust since the dust in such systems is near sites of active star formation or active nuclei. Moreover, galaxies that appear as several bright clumps in the infrared such as Holmberg II provide a large number of low optical depth lines of sight from which ultraviolet photons may escape (or their ultraviolet emission does not come from a single burst, but is rather more continuous or multigenerational in nature). Such clumpy galaxies would hence show comparatively low infrared-to-ultraviolet ratios. On the other hand, ultraviolet photons from galaxies that appear in the infrared as a single pointlike blob of nuclear emission (e.g., NGC 1266) would encounter significant extinction, and hence such galaxies would

exhibit high infrared-to-ultraviolet ratios and high dust temperatures. In contrast to hot dust systems, galaxies with relatively low $f_\nu(70\ \mu m)/f_\nu(160\ \mu m)$ ratios have cooler dust because the dust is not in spatial proximity of the hot stars (e.g., Panagia 1973). The heating of dust via the weaker ambient interstellar radiation field would be fractionally higher in these galaxies. Therefore, their morphological appearance in the infrared should be comparatively smooth (e.g., NGC 2841).

Since the relative distribution of interstellar grains and their heating sources is central to the scenario outlined above, we turn to the 24 μm morphology of SINGS galaxies to provide a test of the above scenario. MIPS 24 μm data may be uniquely suited for such a test, as the data have significantly higher spatial resolution than either 70 or 160 μm imaging (the $6''$ 24 μm beam corresponds to ~ 0.3 kpc at 10 Mpc) and effectively trace both interstellar grains and active sites of star formation[21] (e.g., Hinz et al. 2004; Gordon et al. 2004). In fact, the 24 μm emission can be spatially closely associated with H II regions and in such cases is probably dominated by dust from *within* these regions (Helou et al. 2004; Murphy et al. 2006). To facilitate our analysis, we have decomposed the 24 μm images into unresolved (point sources) and

---

[21] Note that the 24 μm emission contains up to $\sim 25\%$ stellar emission for many SINGS early-type galaxies.
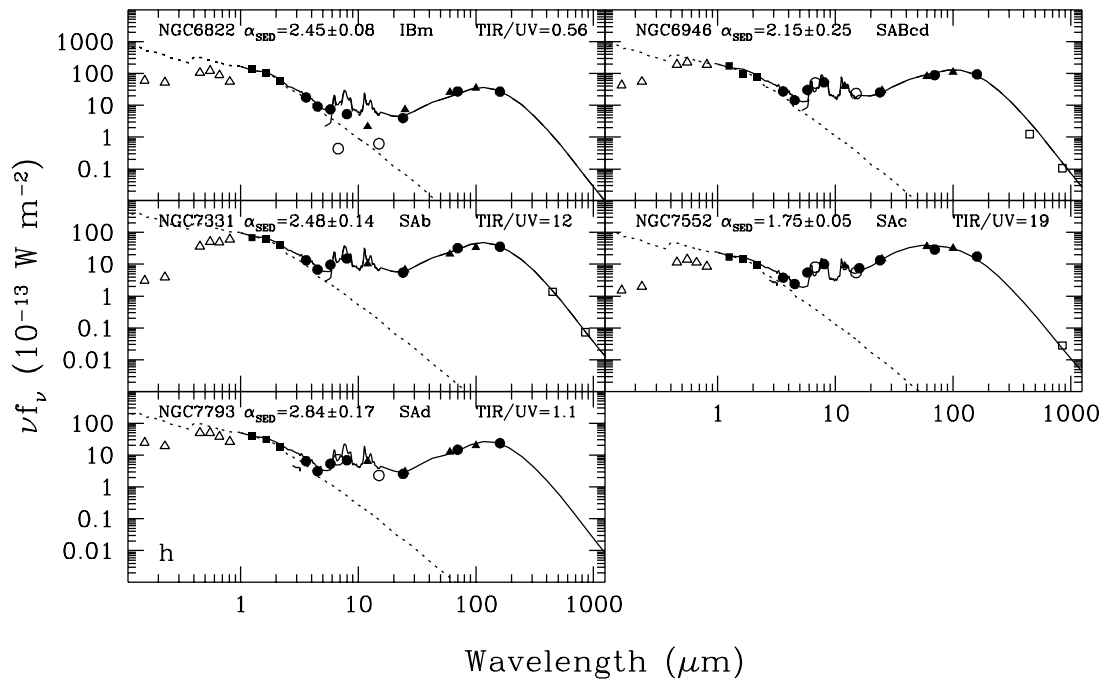
FIG. 1.—Continued

resolved emission. The point-source photometry is done using StarFinder (Diolaiti et al. 2000), which is appropriate for the stable and well-sampled MIPS 24 μm PSF. A STinyTim (Krist 2002) model PSF with a temperature of 100 K, smoothed to account for pixel sampling, is used. Smoothed STinyTim PSFs are excellent matches to observed MIPS 24 μm PSFs (C. W. Engelbracht et al. 2007, in preparation). An image of all of the detected point sources is created along with a difference image made by subtracting the point-source image from the observed image. The fluxes are measured in the point-source ("unresolved") and difference ("resolved") images in the same aperture used for the total galaxy measurement (see Fig. 7). In addition, nuclear fluxes are measured in a 12″ radius circular aperture on the observed image.

The results from this analysis are displayed in Figures 8 and 9. In Figure 8 the symbol size linearly scales with the ratio of unresolved to resolved 24 μm emission, with the largest symbols corresponding to ratios ~10.

In addition, each data symbol reflects the ratio of nuclear to total 24 μm emission, as indicated in the figure legend. Galaxies dominated by a single point source of nuclear emission at 24 μm appear preferentially in the upper right portion of the diagram. These galaxies contain hot dust and show relatively high infrared-to-ultraviolet ratios since the dust is centrally concentrated near the heating sources in the nuclei. Note that nuclear activity is not the main factor in determining the 24 μm morphology: only two of the pointlike systems have active nuclei (NGC 1266 and NGC 5195). Systems with clumpy 24 μm morphologies appearing in the lower right corner still contain hot dust; the dust is concentrated around several heating sources, not just the nuclear ones. Moreover, the clumpy distribution provides a larger number of low τ or "clean" lines of sight for ultraviolet photons to escape the

FIG. 2.—Display of stacked SEDs that emphasizes the infrared-to-ultraviolet variations within the SINGS sample. Each SED in the stack represents an average of approximately 10 individual SEDs that fall within a given bin of the infrared-to-ultraviolet ratio. [*See the electronic edition of the Journal for a color version of this figure.*]
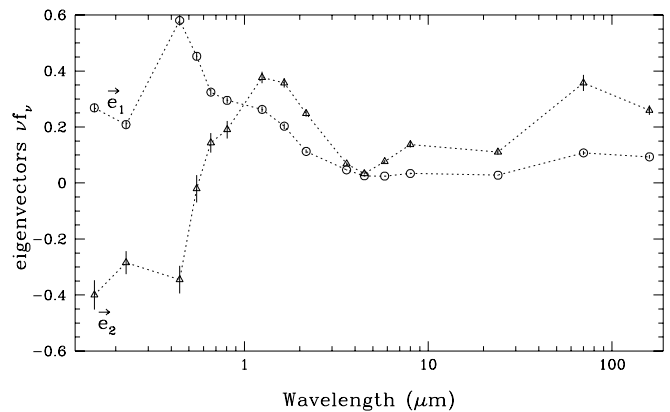
FIG. 3.—Strongest (*circles*) and second strongest (*triangles*) eigenvector spectra from a principal component analysis of the SINGS spectra. These are average eigenvectors stemming from 10,000 Monte Carlo simulations based on the observed fluxes and their uncertainties (corrected for Galactic extinction and air mass in the case of ground-based observations); the error bars shown in this figure indicate the dispersion of the eigenspectra from the simulations. These eigenvectors have normalized eigenvalues of 0.88 and 0.07; $\langle e_1 \rangle$ and $\langle e_2 \rangle$, respectively, contribute to 88% and 7% of the observed variation in the sample spectra. [*See the electronic edition of the Journal for a color version of this figure.*]
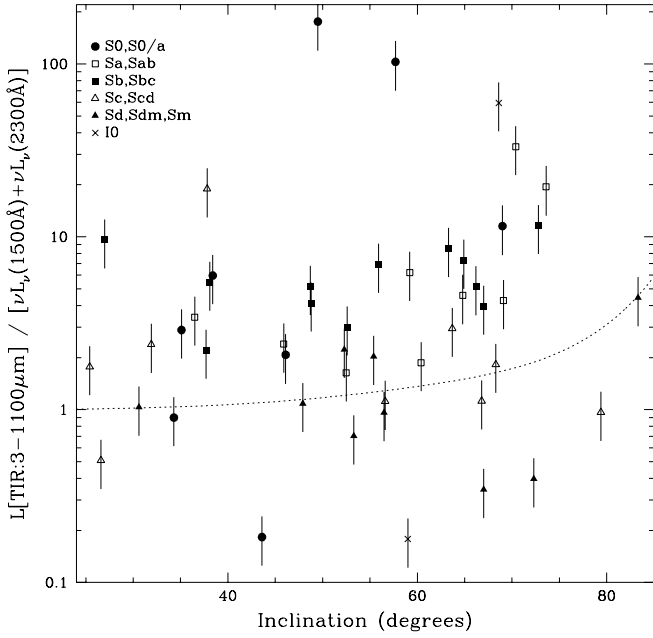
FIG. 4.—Infrared-to-ultraviolet ratio as a function of galaxy disk inclination. The dotted line, normalized to an infrared-to-ultraviolet ratio of unity at zero inclination, shows the expected effect of extinction on the ultraviolet data with changing inclination using the thin-disk model and a central face-on optical depth in the B band of $\tau_B^f = 2$ described in Tuffs et al. (2004). The error bars stem from the observational uncertainties.

FIG. 6.—Infrared-to-ultraviolet ratio as a function of far-infrared color for the SINGS sample. Data from the *GALEX* Atlas of Nearby Galaxies (Gil de Paz et al. 2007) are also shown as small data points without error bars. [*See the electronic edition of the Journal for a color version of this figure.*]

galaxies, decreasing their infrared-to-ultraviolet ratios (see, for example, Roussel et al. 2005). Finally, galaxies with smoother 24 μm morphologies exhibit cooler far-infrared colors. To see the latter effect more clearly, we show in Figure 9 the ratio of unresolved-to-resolved 24 μm emission as a function of far-infrared color. Clearly there is a trend, indicating that the 24 μm morphology can, for nearby galaxies, indicate the relative separation be-

tween interstellar grains and their heating sources. Note that distance contributes but does not dominate as a driver for the effect (the symbol sizes are scaled according to galaxy distance).

5.4. *Specific Star Formation Rate*

One way to parameterize the star formation history of a galaxy is via the star formation rate per stellar mass, or the specific star formation rate (SSFR). Drory et al. (2004) and Feulner et al. (2005), for example, have utilized the specific star formation rate to explore the role of star formation in the growth of stellar mass over cosmic timescales. In this work the specific star formation rate is quantified as a combination of the observed infrared and far-ultraviolet luminosities:

$$\text{SSFR}\left(\text{yr}^{-1}\right) \simeq \frac{4.5\text{TIR}(10^{37}\ \text{W}) + 7.1\nu L_\nu\left(1500\ \text{\AA}\right)(10^{37}\ \text{W})}{0.8\nu L_\nu(K_s)\ (L_\odot)},$$

(6)

based on star formation rate conversion factors from Kennicutt (1998). The numerator in equation (6), applicable for galaxies with continuous star formation occurring on timescales $\gtrsim 10^8$ yr, is a more robust way to quantify the star formation rate than relations that are limited to either infrared or ultraviolet luminosities. The infrared luminosity accurately corresponds to the star formation rate only in the limiting case where all of the star formation–related stellar emission is captured by interstellar dust grains. Similarly, the ultraviolet emission can also be a poor measure of the star formation rate, especially when extinction is significant. However, combining both the ultraviolet and infrared luminosities in equation (6) is akin to an extinction-corrected ultraviolet luminosity and thus more effectively recovers the true star formation rate (see also Bell 2003; Iglesias-Páramo et al. 2006). We note that similar values are obtained when using the optimal infrared+ultraviolet star formation rate tracer determined by Hirashita et al. (2003; their eq. [25]), which incorporates parameters that account for the fraction of Lyman continuum luminosity ($f \simeq 0.57$), the
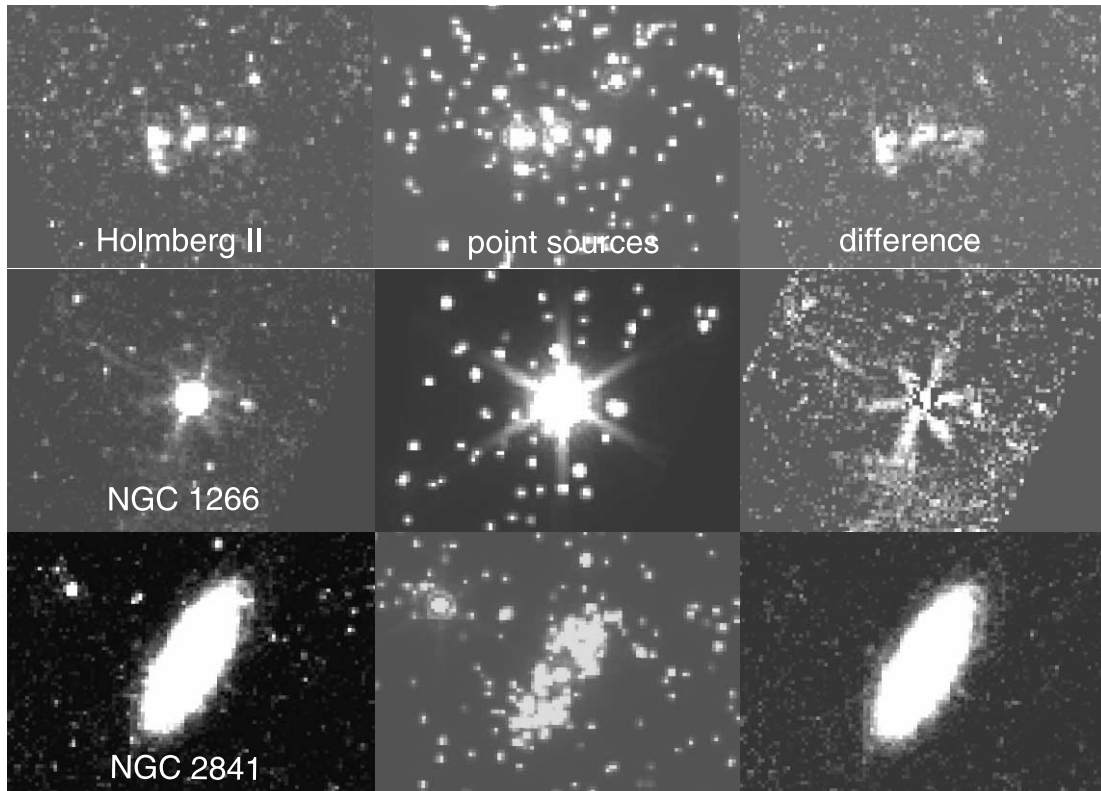

FIG. 5.—Infrared-to-ultraviolet ratio as a function of galaxy optical morphology. The equation provided quantifies the approximate trend with Hubble type for late-type galaxies shown as a dotted line (e.g., Sa → T = 1, Sb → T = 3, Sc → T = 5, etc.).

FIG. 7.—Examples of galaxies with clumpy (Holmberg II), unresolved (NGC 1266), and smooth (NGC 2841) 24 μm emission. The left, middle, and right panels, respectively, show the original 24 μm images, images of the point sources therein, and the differences in the original and point-source images (see § 5.3). The images are approximately 700″ across (~12, ~100, and ~35 kpc for Holmberg II, NGC 1266, and NGC 2841, respectively).

fraction of ultraviolet luminosity absorbed by dust ($\epsilon \simeq 0.53$), and the fraction of dust heating by stellar populations older than 10^8 yr ($\eta \simeq 0.40$). The K_s band luminosity in the denominator of equation (6) is equivalent to a stellar mass. Bell et al. (2003), for example, fit stellar population synthesis models to thousands of

2MASS plus Sloan Digital Sky Survey optical–near-infrared data sets and find that the distribution of M_*/L_{K_s} peaks near ~0.8 $M_\odot L_\odot^{-1}$ for a wide range of galactic masses. Gavazzi et al. (1996) also show that the dynamical mass in a galaxy is proportional to the H-band luminosity.
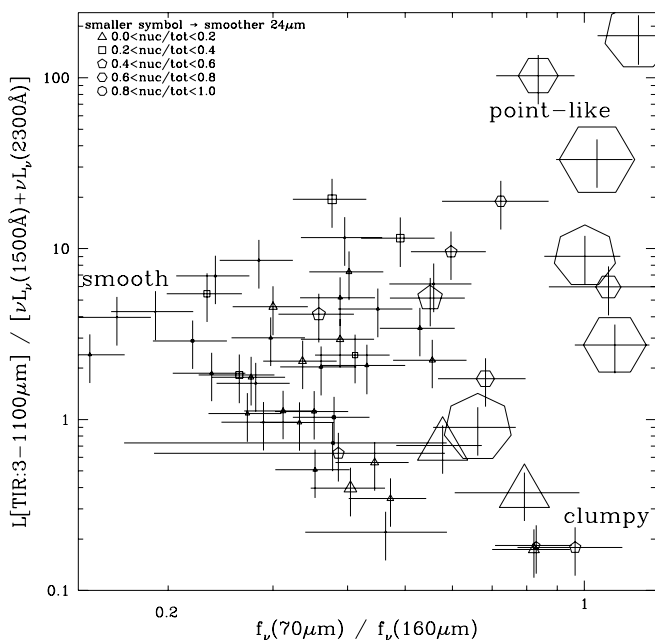
FIG. 8.—Similar to Fig. 6, but with symbol size scaled according to the ratio of unresolved to resolved 24 μm emission; the largest symbols have this ratio equal to ~10. Each data point is also symbolized according to the ratio of nuclear to total 24 μm emission (see § 5.3).
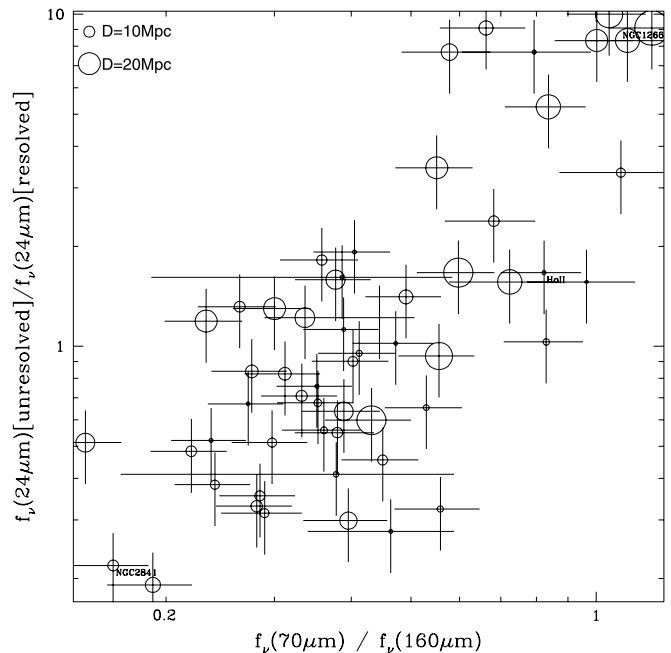
FIG. 9.—Ratio of unresolved to resolved 24 μm emission as a function of far-infrared color (see § 5.3). A 25% uncertainty is used for the error bars in the unresolved-to-resolved ratio. The symbol sizes are scaled according to galaxy distance (see legend).
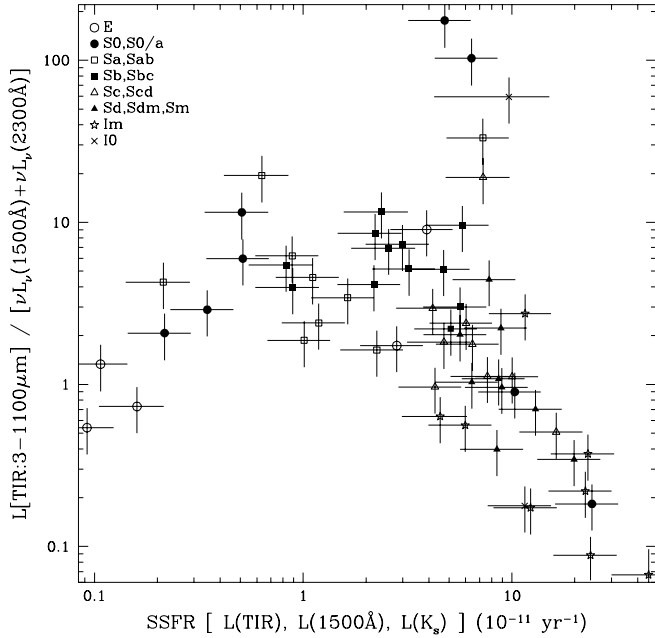
Fig. 10.—Infrared-to-ultraviolet ratio as a function of the specific star formation rate (eq. [6]). The error bars derive from the observational uncertainties plus a 30% factor assumed for converting the K_s luminosity to a stellar mass (see § 5.4).

Fig. 11.—Infrared–to–far-ultraviolet ratio as a function of H-band luminosity. The dotted line is a fit "by eye" to the general trend.

Figure 10 presents the interplay between the specific star formation rate, the infrared-to-ultraviolet ratio, and optical morphology. With the exception of a handful of nuclear 24 μm sources with high infrared-to-ultraviolet ratios, the SINGS sample shows a general trend in this diagram. Galaxies with low specific star formation rates (SSFR $\lesssim$ 0.9 yr^{-1}) are of E, S0, S0/a, or Sa morphologies, consistent with the traditional notion that early-type galaxies exhibit low star formation rates per unit stellar mass (see, e.g., Sandage 1986). These early-type galaxies show increasing infrared-to-ultraviolet ratios for increasing specific star formation rates. In contrast, spiral galaxies generally show SSFR $\gtrsim$ 0.9 yr^{-1}, and the later the spiral Hubble type, the larger the specific star formation rate and the smaller the infrared-to-ultraviolet ratio. Note that the numerator in equation (6) overestimates the star formation rate for early-type galaxies, since the bulk of their infrared and ultraviolet luminosities are not due to recently formed stars.

Assuming that equation (6) can be reasonably applied to the SINGS early-type galaxies, in order to observe larger infrared-to-ultraviolet ratios (and thus larger dust extinction), increases in the specific star formation must be associated with increased amounts of interstellar dust. On the other hand, increasing the specific star formation rate in late-type galaxies results in smaller infrared-to-ultraviolet ratios: the additional ultraviolet photons in spiral galaxies with high SSFRs tend to more easily escape the galaxies, since their clumpy distribution of dust provides many more sight lines of low optical depth than found in 24 μm–smooth early-type galaxies. In other words, the increased star formation rate in later type spiral galaxies must lead to a higher density of holes through which ultraviolet photons can escape.

5.5. Luminosity

Global parameters related to galaxy structure, star formation history, molecular and atomic gas content, metallicity, etc., are known to trend with H-band luminosity, another popular proxy for galaxy stellar mass, especially for late-type galaxies (e.g., Gavazzi et al. 1996; Boselli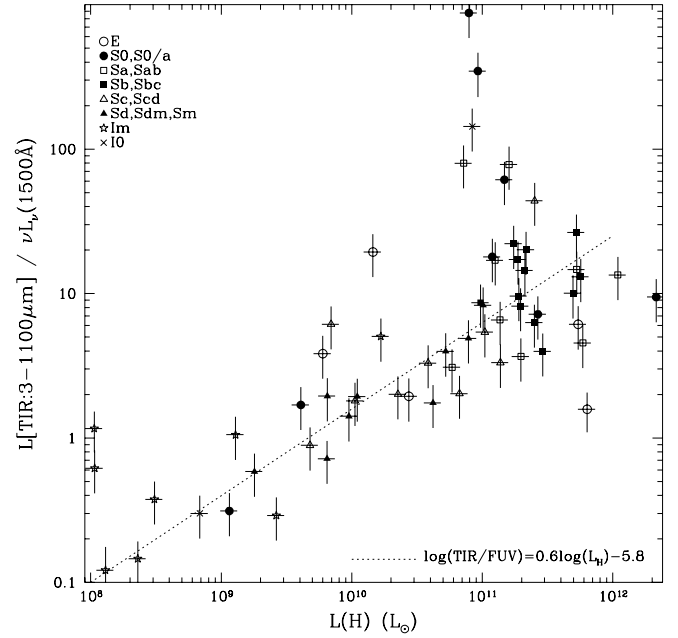 et al. 2001). Figure 11 displays the infrared–to–far-ultraviolet ratio versus 2MASS H-band luminosity. A clear correlation is found: more luminous (massive) galaxies show larger infrared–to–far-ultraviolet ratios, consistent with the findings of Cortese et al. (2006). Although most of the low-luminosity dwarfs and early-type galaxies follow the general trend, the data for E and S0/S0a galaxies contribute to increased scatter at high luminosity. This increased scatter for early-type galaxies is not surprising given the large dispersion for these types of galaxies seen in Figure 5 and since the ultraviolet-emitting stars in the most massive early-type galaxies are generally associated with an old stellar population (see Boselli et al. 2005). Although the older stars might also contribute to the dust heating in massive early-type galaxies, the spectral shapes in Figure 1 suggest that the bulk of the dust heating in these systems is dominated by intermediate-age stars emitting mostly in the visible. In contrast, the spectral shapes for most later type galaxies in Figure 1 indicate that the bulk of the dust heating is being carried out by a younger (bluer) stellar population.

5.6. Ultraviolet Spectral Slope

The infrared-to-ultraviolet ratio has been shown to be fairly tightly correlated with the ultraviolet spectral slope in starburst galaxies, an important discovery that allows the extinction at ultraviolet wavelengths to be estimated from ultraviolet spectral data alone (e.g., Calzetti et al. 1994; Calzetti 1997; Meurer et al. 1999). A starburst galaxy is defined here as a galaxy experiencing prodigious, recent star formation (perhaps triggered by an encounter) at a rate that cannot be sustained over the lifetime of the galaxy. Nonstarbursting galaxies have also been studied in the context of infrared-to-ultraviolet ratio and ultraviolet spectral slope, but their data show a larger dispersion, with normal star-forming and quiescent systems exhibiting redder ultraviolet spectra and/or lower infrared-to-ultraviolet ratios (e.g., Buat et al. 2002, 2005; Bell 2002; Kong et al. 2004; Gordon et al. 2004; Burgarella et al. 2005; Calzetti et al. 2005; Seibert et al. 2005; Cortese et al. 2006; Boissier et al. 2007; Gil de Paz et al. 2007). The intrinsic ultraviolet spectral slope is quite sensitive to the effective age of the stellar population, leading Calzetti et al. (2005)
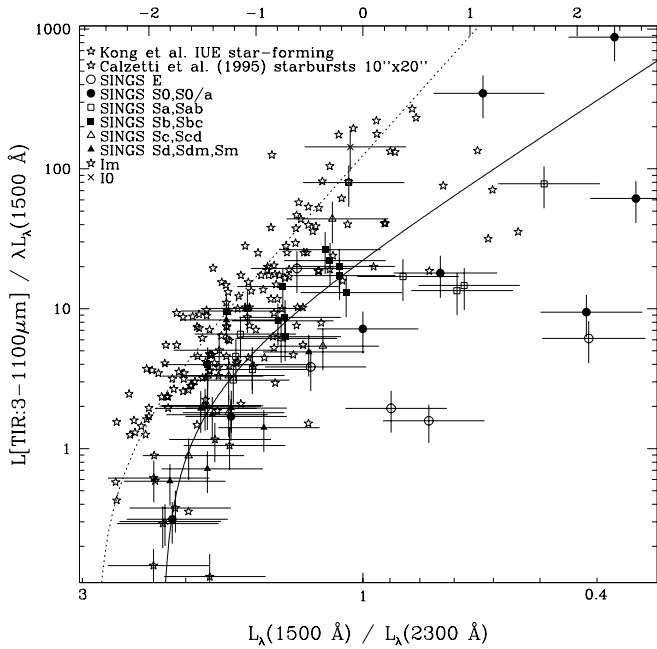
FIG. 12.—Infrared–to–far-ultraviolet ratio as a function of ultraviolet spectral slope. Normal star-forming and starbursting galaxies from Kong et al. (2004) and Calzetti et al. (1995) are plotted in addition to the SINGS data points. The dotted line is that for starbursting galaxies from Kong et al. (2004), and the solid line is applicable to normal star-forming galaxies (Cortese et al. 2006). [*See the electronic edition of the Journal for a color version of this figure.*]

to suggest that the evolved, nonionizing stellar population ($\sim$50–100 Myr) dominates the ultraviolet emission in normal systems, in contrast to current star formation processes dominating the ultraviolet emission in starbursts. The increased diversity in the ultraviolet spectral slopes for evolved stellar populations manifests itself as a larger dispersion for quiescent and normal star-forming galaxies in plots of the infrared-to-ultraviolet ratio as a function of ultraviolet spectral slope. Interestingly, Boissier et al. (2007) use azimuthally averaged radial profiles, and after excluding emission from the bulge/nucleus, they find that the relation between infrared-to-ultraviolet and ultraviolet slope tightens up compared with the one obtained using the integrated data. This result is consistent with the interpretation of Calzetti et al. (2005) either if the evolved stellar populations in normal star-forming galaxy bulges cause the increased scatter compared to the starburst trend or if azimuthally averaging smooths over small-scale effects such as the heating of dust in one region by ultraviolet light from a different nearby region.

Figure 12 displays a diagram of spatially integrated infrared-to-ultraviolet ratios and ultraviolet spectral slopes. Normal star-forming and starbursting galaxies from Kong et al. (2004) and Calzetti et al. (1995) are plotted in addition to the SINGS data points. The dotted line is that for starbursting galaxies from Kong et al. (2004), and the solid line is applicable to normal star-forming galaxies of type Sa or later (Cortese et al. 2006). Similar to what has been found for other samples of nonstarbursting galaxies, the SINGS data set shows more scatter in this diagram and the galaxies are redder in their ultraviolet spectral slope compared to starburst galaxies. Inspection of the distribution as a function of SINGS optical morphology, however, shows that the 14 reddest SINGS galaxies are type Sab or earlier, a result that is perhaps expected for systems with quenched star formation rate histories; the early-type galaxies in SINGS contribute to most of the observed scatter, such that the trend for the subset of just late-type SINGS galaxies shows a dispersion comparable to that for star-

bursts. The 14 reddest SINGS galaxies also significantly differ from even the normal galaxy curve, but this is consistent with the fact that Cortese et al. (2006) excluded types earlier than Sa for their analysis. Finally, although the SINGS sample shows very large dispersion and does not as a whole match the starburst trend, we have verified that the starburst subset of SINGS (e.g., Mrk 33, NGC 1705, NGC 2798, NGC 3034, NGC 7552) does indeed match the canonical starburst trend.

6. DISCUSSION AND SUMMARY

The ultraviolet-to-radio broadband SEDs are presented for the 75 galaxies in the *Spitzer* Infrared Nearby Galaxies Survey, a collection of galaxies that broadly samples the wide variety of galaxy morphologies, luminosities, colors, and metallicities seen in the local universe. The infrared-to-ultraviolet ratio is explored in conjunction with several global parameters. An interesting empirical finding is that systems with cooler dust show a restricted range of infrared-to-ultraviolet ratios ($\sim$0.5 dex), while systems with warm global far-infrared colors exhibit a large range of infrared-to-ultraviolet ratios ($\sim$3 dex). To put it another way, the cold dust systems in the SINGS sample show average ultraviolet extinctions; no cold galaxy is particularly optically thick or thin. There remains the possibility that part of this distribution is attributable to selection effects, but we use the morphology from MIPS 24 μm imaging to interpret this distribution to result from the relative distribution of dust grains and their heating sources. Nearby galaxies with globally cooler dust appear smoother at 24 μm, from which we infer that the dust grains are well mixed throughout the interstellar medium and not concentrated near sites of active star formation. On the other hand, galaxies with elevated $f_\nu(70\ \mu m)/f_\nu(160\ \mu m)$ ratios appear as one or a handful of clumps at 24 μm and thus have much of their dust considerably closer to heating sources. The observed range in infrared-to-ultraviolet ratio is also related to the 24 μm morphology, from which the density of available clean lines of sight for ultraviolet photons to escape can be inferred. The dust distribution in galaxies appearing as a single clump at 24 μm heavily enshrouds the heating sources (high infrared-to-ultraviolet ratios), galaxies with multiple clumps at 24 μm provide a large number of low optical depth lines of sight along which ultraviolet photons can escape (low infrared-to-ultraviolet ratios), and a smooth distribution at 24 μm implies a dust distribution that provides an intermediate number of low optical depth lines of sight (average infrared-to-ultraviolet ratios). Detailed studies of the relative distributions of the infrared emission and the ionizing radiation fields in SINGS galaxies have been carried out in IC 2574 (Cannon et al. 2005), NGC 1705 (Cannon et al. 2006a), and NGC 6822 (Cannon et al. 2006b). These dwarf galaxies appear as multiple clumps at 24 μm and show low optical extinctions and highly variable ratios of Hα to infrared (i.e., significant ultraviolet photon leakage), consistent with our expectation that multiclump 24 μm galaxies should have warm far-infrared colors and low global infrared-to-ultraviolet ratios.

A principal component analysis of the SINGS broadband spectra indicates that most of the sample's large broadband spectral variations stem from two underlying components, one typical of a galaxy with a low infrared-to-ultraviolet ratio (88% of the sample variation) and one indicative of a galaxy with a high infrared-to-ultraviolet ratio (7% of the sample variation). The implication is that the star formation history (i.e., the specific star formation rate, the birthrate parameter, or some other measure of the current to past star formation rate) may be the dominant regulator of the broadband spectral variations between galaxies. From a morphological standpoint, we find that much of the dispersion in plots

such as infrared-to-ultraviolet versus ultraviolet spectral slope (Fig. 12) stems from early-type galaxies, which have significantly redder ultraviolet spectra than other galaxy types. In fact, the galaxies with the highest optical-to-infrared ratios, the smallest specific star formation rates, and the reddest ultraviolet slopes are all early-type galaxies (see Figs. 1, 10, and 12, respectively).

Evidence for the star formation history regulating spectral variations is found in a striking trend in the infrared-to-ultraviolet ratio as a function of the specific star formation rate (Fig. 10). Early-type galaxies show higher ratios of infrared to ultraviolet (higher dust extinction) for larger specific star formation rates, implying that the specific star formation rate in elliptical and S0 galaxies is closely tied to the *amount* of dust. Conversely, spiral galaxies show lower infrared-to-ultraviolet ratios (lower dust extinction) for higher specific star formation rates, suggesting that the specific star formation rate in elliptical galaxies is linked to the *distribution* of dust: in spiral galaxies a larger number of holes are created for increased star formation activity, holes through which ultraviolet light more easily passes out of galaxies.

In a study of 99,088 galaxies from the Sloan Digital Sky Survey, Obrić et al. (2006) find that the *GALEX*, Sloan, and 2MASS data "form a nearly one parameter family." In particular, they can predict with 20% accuracy the 2MASS K_s flux using just the Sloan *u* and *r* fluxes. In addition, they can predict to within a factor of 2 certainty the *IRAS* 60 μm flux based on the Sloan broadband data. Such simple optical-infrared correlations are not seen for SINGS galaxies. However, Obrić et al. (2006) are only able to identify *IRAS* fluxes for less than 2% of their sample, and this subset is strongly biased to optically blue galaxies. The SINGS sample, although far smaller in size, provides complete panchromatic information for a far more diverse ensemble of galaxies and is thus much less biased to a particular subset of the local galaxy population.

REFERENCES

Adelberger, K. L., & Steidel, C. C. 2000, ApJ, 544, 218
Bauer, F. E., Condon, J. J., Thuan, T. X., & Broderick, J. J. 2000, ApJS, 129, 547
Bell, E. F. 2002, ApJ, 577, 150
———. 2003, ApJ, 586, 794
Bell, E. F., Gordon, K. D., Kennicutt, R. C., & Zaritsky, D. 2002, ApJ, 565, 994
Bell, E. F., McIntosh, D. H,, Katz, N., & Weinberg, M. D. 2003, ApJS, 149, 289
Boissier, S., et al. 2007, ApJ, in press
Boselli, A., & Gavazzi, G. 1994, A&A, 283, 12
Boselli, A., Gavazzi, G., Donas, J., & Scodeggio, M. 2001, AJ, 121, 753
Boselli, A., Gavazzi, G., & Sanvito, G. 2003, A&A, 402, 37
Boselli, A., et al. 2005, ApJ, 629, L29
Bruzual, A. G., Magris, G., & Calvet, N. 1988, ApJ, 333, 673
Buat, V., Boselli, A., Gavazzi, G., & Bonfanti, C. 2002, A&A, 383, 801
Buat, V., & Xu, C. 1996, A&A, 306, 61
Buat, V., et al. 2005, ApJ, 619, L51
Burgarella, D., Buat, V., & Iglesias-Páramo, J. 2005, MNRAS, 360, 1413
Calzetti, D. 1997, AJ, 113, 162
Calzetti, D., Bohlin, R. C., Kinney, A. L., Storchi-Bergmann, T., & Heckman, T. M. 1995, ApJ, 443, 136
Calzetti, D., Kinney, A. L., & Storchi-Bergmann, T. 1994, ApJ, 429, 582
Calzetti, D., et al. 2005, ApJ, 633, 871
Cannon, J. M., et al. 2005, ApJ, 630, L37
———. 2006a, ApJ, 647, 293
———. 2006b, ApJ, 652, 1170
Chapman, S. C., Smail, I., Ivison, R. J., Helou, G., Dale, D. A., & Lagache, G. 2002, ApJ, 573, 66
Condon, J. J. 1987, ApJS, 65, 485
Condon, J. J., Cotton, W. D., Greisen, E. W., Yin, Q. F., Perley, R. A., Taylor, G. B., & Broderick, J. J. 1998, AJ, 115, 1693
Condon, J. J., Helou, G., Sanders, D. B., & Soifer, B. T. 1990, ApJS, 73, 359
Cortese, L., et al. 2006, ApJ, 637, 242
Dale, D. A., Giovanelli, R., Haynes, M. P., Scodeggio, M., Hardy, E., & Campusano, L. E. 1997, AJ, 114, 455
Dale, D. A., & Helou, G. 2002, ApJ, 576, 159
Dale, D. A., Helou, G., Contursi, A., Silbermann, N. A., & Kolhatkar, S. 2001, ApJ, 549, 215
Dale, D. A., et al. 2005, ApJ, 633, 857
Deeming, T. F. 1964, MNRAS, 127, 493
de Vaucouleurs, G., de Vaucouleurs, A., Corwin, H. G., Buta, R. J., Paturel, G., & Fouqué, P. 1991, Third Reference Catalogue of Bright Galaxies (New York: Springer)

Diolaiti, E., Bendinelli, O., Bonaccini, D., Close, L., Currie, D., & Parmeggiani, G. 2000, A&AS, 147, 335
Draine, B. T. 2003, ARA&A, 41, 241
Drory, N., Bender, R., Feulner, G., Hopp, U., Maraston, C., Snigula, J., & Hill, G. J. 2004, ApJ, 608, 742
Engelbracht, C. W., Gordon, K. D., Rieke, G. H., Werner, M. W., Dale, D. A., & Latter, W. B. 2005, ApJ, 628, L29
Feulner, G., Goranova, Y., Drory, N., Hopp, U., & Bender, R. 2005, MNRAS, 358, L1
Fukugita, M., Nakamura, O., Turner, E. L., Helmboldt, J., & Nichol, R. C. 2004, ApJ, 601, L127
Galliano, F., Madden, S. C., Jones, A. P., Wilson, C. D., & Bernard, J. P. 2005, A&A, 434, 867
Gavazzi, G., Pierini, D., & Boselli, A. 1996, A&A, 312, 397
Gil de Paz, A., et al. 2007, ApJ, in press
Giovanelli, R., Haynes, M. P., Salzer, J. J., Wegner, G., da Costa, L. N., & Freudling, W. 1995, AJ, 110, 1059
Gordon, K. D., Clayton, G. C., Witt, A. N., & Misselt, K. A. 2000, ApJ, 533, 236
Gordon, K. D., et al. 2004, ApJS, 154, 215
Helou, G., et al. 2004, ApJS, 154, 253
Hinz, et al. 2004, ApJS, 154, 259
Hirashita, H., Buat, V., & Inoue, A. K. 2003, A&A, 410, 83
Hummel, E. 1980, A&AS, 41, 151
Hunter, D. A., & Gallagher, J. S., III 1986, PASP, 98, 5
Iglesias-Páramo, J., et al. 2006, ApJS, 164, 38
Inoue, A. K., Buat, V., Burgarella, D., Panuzzo, P., Takeuchi, T. T., & Iglesias-Páramo, J. 2006, MNRAS, 370, 380
Jarret, T. H., Chester, T., Cutri, R., Schneider, S. E., & Huchra, J. P. 2003, AJ, 125, 525
Kennicutt, R. C. 1998, ARA&A, 36, 189
Kennicutt, R. C., et al. 2003, PASP, 115, 928
Kong, X., Charlot, S., Brinchmann, J., & Fall, S. M. 2004, MNRAS, 349, 769
Krist, J. 2002, Tiny Tim/*SIRTF* User's Guide (Pasadena: Spitzer Science Center)
Kroupa, P. 2002, Science, 295, 82
Kuchinski, L. E., Terndrup, D. M., Gordon, K. D., & Witt, A. N. 1998, AJ, 115, 1438
Li, A., & Draine, B. T. 2001, ApJ, 554, 778
Martin, D. C., et al. 2005, ApJ, 619, L1
Meurer, G. R., Heckman, T. M., & Calzetti, D. 1999, ApJ, 521, 64

Murphy, E. J., et al. 2006, ApJ, 638, 157
Obrić, M., et al. 2006, MNRAS, 370, 1677
O'Connell, R. W. 1999, ARA&A, 37, 603
Panagia, N. 1973, AJ, 78, 929
Rich, R. M., et al. 2005, ApJ, 619, L107
Roussel, H., Gil de Paz, A., Seibert, M., Helou, G., Helou, G., Madore, B. F., &
    Martin, C. 2005, ApJ, 632, 227
Roussel, H., Helou, G., Beck, R., Condon, J. J., Bosma, A., Matthews, K., &
    Jarrett, T. H. 2003, ApJ, 593, 733
Rowan-Robinson, M., et al. 2005, AJ, 129, 1183
Sajina, A., Scott, D., Dennefeld, M., Dole, H., Lacy, M., & Lagache, G. 2006,
    MNRAS, 369, 939
Sandage, A. 1986, A&A, 161, 89
Schlegel, D. J., Finkbeiner, D. P., & Davis, M. 1998, ApJ, 500, 525

Schmitt, H. R., Calzetti, D., Armus, L., Giavalisco, M., Heckman, T. M.,
    Kennicutt, R. C., Leitherer, C., & Meurer, G. R. 2006, ApJ, 643, 173
Seibert, M., et al. 2005, ApJ, 619, L55
Tuffs, R. J., Popescu, C. C., Völk, H. J., Kylafis, N. D., & Dopita, M. A. 2004,
    A&A, 419, 821
van Zee, L., Haynes, M. P., & Salzer, J. J. 1997, AJ, 114, 2479
Vazquez, G. A., & Leitherer, C. 2005, ApJ, 621, 695
Walter, F., et al. 2006, ApJ, submitted
Wright, A., & Otrupcek, R. 1990, Parkes Catalogue (Australian Telescope
    National Facility)
Xilouris, E. M., Madden, S. C., Galliano, F., Vigroux, L., & Sauvage, M. 2004,
    A&A, 416, 41
Yi, S. K., et al. 2005, ApJ, 619, L111
Yun, M. S., Reddy, N. A., & Condon, J. J. 2001, ApJ, 554, 803